

# Coercivity influence of nanostructure in SmCo-1:7 magnets: Machine learning of high-throughput micromagnetic data

Yangyiwei Yang<sup>1,\*</sup>, Patrick Kühn<sup>1</sup>, Mozhdeh Fathidoost<sup>1,\*</sup>, Esmaeil Adabifiroozjahi<sup>3</sup>, Ruiwen Xie<sup>4</sup>, Eren Foya<sup>1</sup>, Dominik Ohmer<sup>4</sup>, Konstantin Skokov<sup>5</sup>, Leopoldo Molina-Luna<sup>2</sup>, Oliver Gutfleisch<sup>5</sup>, Hongbin Zhang<sup>3</sup>, and Bai-Xiang Xu<sup>1,\*</sup>

<sup>1</sup>Mechanics of Functional Materials Division, Institute of Materials Science, Technische Universität Darmstadt, Darmstadt 64287, Germany

<sup>2</sup>Advanced Electron Microscopy Division, Institute of Materials Science, Technische Universität Darmstadt, Darmstadt 64287, Germany

<sup>3</sup>Theory of Magnetic Materials Division, Institute of Materials Science, Technische Universität Darmstadt, Darmstadt 64287, Germany

<sup>4</sup>VACUUMSCHMELZE GmbH & Co. KG, 63450 Hanau, Germany

<sup>5</sup>Functional Materials (FM), Materials Science Department, Technical University of Darmstadt, 64287 Darmstadt, Germany

\*Corresponding authors: [xu@mfm.tu-darmstadt.de](mailto:xu@mfm.tu-darmstadt.de) (Bai-Xiang Xu), [yangyiwei.yang@mfm.tu-darmstadt.de](mailto:yangyiwei.yang@mfm.tu-darmstadt.de) (Yangyiwei Yang), [mozhdeh.fathidoost@mfm.tu-darmstadt.de](mailto:mozhdeh.fathidoost@mfm.tu-darmstadt.de) (Mozhdeh Fathidoost)

## Abstract

Around 17,000 micromagnetic simulations were performed with a wide variation of geometric and magnetic parameters of different cellular nanostructures in the samarium-cobalt-based 1:7-type (SmCo-1:7) magnets. A forward prediction neural network (NN) model is trained to unveil the influence of these parameters on the coercivity of materials, along with the sensitivity analysis. Results indicate the important role of the 1:5-phase in enhancing coercivity. Moreover, an inverse design NN model is obtained to suggest the nanostructure for a queried coercivity.

Samarium-cobalt-based 1:7-type magnet, usually formulated as  $\text{Sm}(\text{Co}, \text{Fe}, \text{Cu}, \text{Zr})_{7\pm\delta}$ , is known as a pinning-controlled permanent magnet that is capable of operating at elevated temperatures. Its corrosion endurance makes it indispensable for high-speed, high-power electric vehicles and aeronautic applications [1–3]. Improving the operational performance of SmCo-based 1:7-type magnet (herein after as SmCo-1:7 magnet) receives continuous attention in the field of rare-earth-containing permanent magnets, as the potential of the materials as defined by crystalline anisotropy is not fully utilized (known as the Brown paradox). The materials optimization relies on the understanding of synthesis-microstructure-performance relationships. A sintered SmCo-1:7 magnet presents a sophisticated microstructure with features spanning multiple length scales, ranging from the mesoscopic (1~100  $\mu\text{m}$ ) polycrystalline texture to the nanoscopic (1~100 nm) three-phase composite [4–6]. As shown in the Fig. 1a, this nanostructure takes a bi-pyramidal or diamond shape, consisting of a stripe-shaped  $\text{Sm}(\text{Co}, \text{Cu})_5$  (hereinafter as 1:5-phase) and a cellular volume filled with  $\text{Sm}_2(\text{Co}, \text{Fe})_{17}$  (2:17-phase). Further subdivisions are created by the presence of Zr-rich platelet (Z-phase) developed perpendicular to the  $c$ -axis [7], intersecting both 2:17-volume and 1:5-boundary of the diamond formation. By merit of high-resolution characterization like high angle annular dark field scanning TEM (HAADF-STEM) imaging, one can observe the atomic stacking and coherent interfaces among these solid-state phases, as shown in Fig. 1b. As its length scale approaches the characteristic length of the magnetic domain-wall dynamics (notably the minimum domain-wall width among the consisting phases) and

existing differences in domain-wall energy among conjugated phases, intersections of these solid-state phases are suggested as effective pinning sites (shown in Fig. 1c), where the additional energy fluctuation is accompanied by further domain-wall motion [8]. Therefore, control and tailoring such nanostructures form a key path leading to the engineering of ideal pinning sites.

Optimizing the micro- and nanostructure to enhance the coercivity of SmCo-1:7 permanent magnets is desired, particularly the geometric and magnetic features of the nanostructure, as it connects process parameters/conditions to the resulting local magnetic hysteresis. This delicate nanostructure is known as a collective outcome of its quinary chemical composition [4–6] and the thermal treatment [7, 9–13]. Among the alloying elements, Zr is crucial for forming of platelet-shape Z-phase and stabilizing of the cellular 2:17-phase [14, 15], while Fe is for improving saturation magnetization and Cu provides concentration gradients in 1:5-phases [8, 16]. Variations in the chemical composition lead to changes not only in the geometry and the topology of nanostructures but also in the magnetic properties of these solid-state phases [17], eventually varying the strength of pinning sites.

Existing works [8, 11–13, 18–33] have defined characteristic quantities to describe phase formation and magnetic properties (notably, domain-wall width and energy, and saturation magnetization) for marking various samples with corresponding measured coercivities. Based on these works, a forward and an inverse problem are posed: the forward problem concerns the identification of structural/magnetic features that are effective to the desired coercivity; in the inverse problem one aims to identify a specific nanostructure and end-member phases for a prescribed coercivity. In this context, the systematic knowledge extracted from an extensive dataset is of paramount importance in addressing these problems, aligning with the data-driven methodologies [34]. To overcome the inefficient experimental-dominant trial-and-error methodologies, high-throughput micromagnetic simulations are employed to generate comprehensive and volume datasets. The solid physical foundation of micromagnetic simulations also aligns with the requirements of data-driven forward analyses and inverse design powered by machine learning (ML) techniques.

In this work, we conducted extensive micromagnetic simulations to realize data-driven forward and inverse machine learning on the coercivity of SmCo-1:7 permanent magnets and its relationship to nanostructural and magnetic features. According to [4], four features are defined to characterize the nanostructure geometry: the average thickness of 1:5- ( $w_s$ ), the average thickness of Z-phase ( $w_z$ ), the average interval of 1:5- ( $L$ ) as well as that of Z-phases ( $d$ ), as shown in Fig. 1c. These four parameters were summarized (in Supplementary Table 1) from the characterization done in the existing experimental works [8, 11–13, 18–33]. Their distribution vs. Zr atom fraction is shown in Fig. 1d. Besides the nanostructural parameters, we considered the influences of the micromagnetic parameters of these solid-state phases on the resulting hysteresis of the nanostructure. These micromagnetic parameters include the misorientation angle  $\alpha$  (i.e., the angle between the applied magnetic field and the magnetocrystalline easy-axis), the saturation magnetization  $M_s$ , the Bloch domain-wall width  $l_{dw}$  and energy  $\sigma_{dw}$ . Here  $\alpha$  varies from  $0^\circ$  (where the applied magnetic field  $\mathbf{H}_{ext}$  field is along the easy-axis) to  $90^\circ$  (where  $\mathbf{H}_{ext}$  is perpendicular to the easy-axis). It is worth noting that the exchange stiffness  $A_{ex}$  and the magnetocrystalline anisotropy constant  $K_u$  for the uniaxial symmetry (two of the model parameters in a micromagnetic simulation), can be related to  $l_{dw}$  and  $\sigma_{dw}$  by

$$\sigma_{dw} = 4\sqrt{A_{ex}K_u} \quad \text{and} \quad l_{dw} = \pi\sqrt{\frac{A_{ex}}{K_u}}, \quad (1)$$

where SI units are used [35]. Compared to  $A_{ex}$  and  $K_u$ ,  $\sigma_{dw}$  and  $l_{dw}$  are the direct features of the domain wall and can reflect the pinning strength of the corresponding solid-state phase. In this work,  $\sigma_{dw}$ ,  $l_{dw}$ , and  $M_s$  for the Sm-Co (1:5 and 2:17) phases are calculated based on the former measurement of the bulk materials [4, 17, 36]. Due to existing uncertainties, various micromagnetic parameters of Z-phase are examined, including values from the experimental measurement [4], values from density functional theory (DFT) calculations with the composition  $\text{Sm}(\text{Co}_{1.8}\text{Zr}_{0.4})_5$ , and values estimated assuming an identical  $l_{dw}$  as 1:5-phase while taking  $\sigma_{dw}$  and  $M_s$  from Ref.

[4], as listed in Supplementary Table 4. This can shed insights on how sensitive the domain-wall motion is to the magnetic properties in Z-phase, whose boundary with other phase is expected to form effective pinning sites in the magnet.

Nanostructural parameters with determined ranges from previous works (Supplementary Fig. 1) were then screened with a given interval and sampled into in-total 17,500 combinations, containing already three different sets of  $\{M_s^{(Z)}, \sigma_{dw}^{(Z)}, l_{dw}^{(Z)}\}$  and five different  $\alpha$ . After filtering impossible nanostructures (e.g.,  $w_Z > d$ ), 16,805 micromagnetic simulations were carried out in a high-throughput GPU-parallel form with details explained in the *Methods* section. To reduce the variations in simulated coercivity, each simulation contains 5-10 demagnetization half-cycles where the magnetization was reversed from the positive saturation state to the negative one. Then, the coercivity  $H_c$  was read on the averaged  $M$ - $H$  curves for each nanostructure. Meanwhile, the first discontinuity in the averaged curve was interpreted as the depinning field  $H_p$ , indicating the minimum field necessary to overcome the energy barrier provided by the pinning sites [37]. In a homogenous nanostructure,  $H_c$  generally equals  $H_p$ , stating a non-impeded domain-wall motion after nucleation. When the nanostructure is inhomogeneous (like this SmCo-1:7 nanostructure),  $H_c$  is further extended from  $H_p$  due to the impeded domain-wall motion by pinning sites. Therefore, a normalized inhomogeneity factor  $\Phi_p = (H_c - H_p)/H_c$  was evaluated (inset of Fig. 2a), quantifying the pinning effects during domain-wall motion. These calculations were automatically conducted by autonomous multiprocessing scripts on high-throughput micromagnetic results. These scripts are also used to identify numerical errors and perform recalculation automatically, preventing contamination of the dataset. After collecting fully compliant simulation results and curating the dataset, the subsequent data-driven analyses, including the training and evaluation of the ML models for forward prediction and inverse design, were conducted with details also explained in the *Methods* section. The workflow is presented in Fig. 1e.

As an instance, Fig. 2a presents the longitudinal half-cycle of a magnetic hysteresis curve during demagnetization, obtained from a nanostructure with parameters  $w_Z = 3$  nm,  $w_S = 3$  nm,  $d = 50$  nm and  $L = 150$  nm and a grain boundary layer ( $K_u^{(\text{bdy})} \sim 0.01K_u^{(\text{bulk})}$ ). The nucleation and pinning events on the nanostructure vary with the orientation angle, even though the parameters of constituent phases do not change. As shown in the figure, the half-cycle hysteresis curves present varying staging patterns w.r.t. the misorientation angle  $\alpha$ , implying both  $H_c$  and  $\Phi_p$  as functions of  $\alpha$ . Although not obvious at  $\alpha = 0^\circ$ , simulated  $H_c$  receive a considerable contribution from the inhomogeneity when  $\alpha \neq 0$ , which is also confirmed by the statistical angular tendency of  $H_c$  over the complete dataset (Fig. 2b). Notably, the mean value of  $\Phi_p$  reaches a maximum at  $\alpha = 60^\circ$ , implying an existing impeded domain-wall motion together with the rotation of the magnetization. As  $\alpha$  approaches  $90^\circ$ , no  $H_c$  and  $\Phi_p$  are presented due to the complete in-plane rotation of magnetization.

Fig. 2c presents how nanostructural parameters, i.e.,  $L$ ,  $d$ ,  $w_S$  and  $w_Z$ , influence  $H_c$  and  $\Phi_p$  for the case of  $\alpha = 0^\circ$ . To establish the forward prediction, a neural-network (NN) model with multi-layer perception architecture is employed. The corresponding contour surfaces show the trend of  $H_c$  and  $\Phi_p$  on nanostructural parameters, while dots indicate micromagnetic results. In the top row, a general trend of  $H_c$  on nanostructural parameters can be observed, i.e., for given  $w_S$  and  $w_Z$ , increasing  $d$  and decreasing  $L$  lead to the improvement of  $H_c$ . An extended contour plot is presented in Supplementary Fig. 5 demonstrating a more complete view of the trend. Notably, a drastic rise of  $H_c$  occurs in the range  $L \in [30, 50]$  nm when  $w_S$  is sufficiently large, especially when  $(w_S)_{\text{max}} = 15$  nm. Considering the anisotropic field evaluated as

$$H_{\text{ani}} = \frac{2K_u}{\mu_0 M_s}, \quad (2)$$

which is treated ideally as the upper-bound coercivity of a homogeneous bulk material as of the Stoner-Wohlfarth model without contribution from the shape anisotropy [38, 39]. In this regard, 1:5-phase has the highest  $H_{\text{ani}}$  among three phases, while 2:17-phase has the lowest one. We further consider two normalized characteristic thicknesses

$$\varphi_S = \frac{w_S}{L}, \quad \varphi_Z = \frac{w_Z}{d}, \quad (3)$$

adapting physical meaning as the approximated volumetric fraction of 1:5- and Z-phases in an ideal periodic microstructure. In this regard, the nanostructure with large  $w_S$  and small  $L$  suggests a relatively high volume fraction of 1:5-phases with the highest  $H_{\text{ani}}$  among three phases (up to 50%), leading to the drastic rise of  $H_c$ . On the other hand, the bottom row depicts the variation of  $\Phi_p$  w.r.t. nanostructural parameters. The corresponding extended contour plot is also presented in Supplementary Fig. 6. A ridge in  $\Phi_p$  contour exists in the range  $L \in [75, 125]$  nm when  $w_Z$  is small ( $w_Z < 7$  nm), demonstrating a high ratio of inhomogeneity contribution in the coercivity. This ridge gradually shifts to high- $L$  range with growing  $w_Z$ , and a valley in  $\Phi_p$  contour emerges in the range  $L \in [75, 125]$  nm when  $w_Z$  is high. Meanwhile, another ridge emerges in the low  $L$  when  $w_S$  approaches 15 nm. When  $d = w_Z = 11$  nm, the nanostructure is fulfilled only with Z-phase, resulting in zero  $\Phi_p$ .

Recalling Eq. (3), we further examine the trends of  $H_c$  and  $\Phi_p$  on the volume fraction of the solid-state phases, which is presented in Fig. 2d. The contour surface is given by the regression of a thin-plate spline (TPS) surface on a dataset containing 2,450 micromagnetic simulation data (resampled from the complete dataset) and 2,300 predicted data by forward NN model (hereinafter as  $f$ -NN model). We also sample 100 data points each by simulation and prediction and illustrate them together with the contour surface. The top left region with low  $\varphi_Z$  and high  $\varphi_S$  shows the high coercivity. Conversely, regions with high  $\varphi_Z$  and low  $\varphi_S$  exhibit low coercivity. It is coherent with the inference given above that the increasing amount of 1:5-phase, which obtains the highest  $H_{\text{ani}}$  among phases, leads to the increasing coercivity of the nanostructure. Meanwhile, maximum  $H_c$  appears in the nanostructure with almost no Z-phase and 50% 1:5-phase in volume fraction, motivating further investigation in the range  $\varphi_S \geq 0.5$  as a follow-up work. Also, assuming ideal lattice structures inside these phases, one can further relate  $\varphi_Z$  to the atomic fraction of Zr, as shown in Supplementary Table 2. In this regard, Zr composition less than 5 at% can have a relatively evident influence on  $H_c$ . Higher than 5 at%, the increase in  $H_c$  is then dominated by the increase in  $\varphi_S$ . As for  $\Phi_p$ , however, the highest inhomogeneity factor is observed at 50% 1:5-phase and around a 32% Z-phase in volume fraction, overlapping with the isoline indicating Zr composition of 5 at%. This pattern suggests that optimizing the ratios of  $\varphi_S$  and  $\varphi_Z$  can significantly influence the inhomogeneity contribution to coercivity.

Sensitivity analyses based on correlation and permutation feature importance were conducted to identify the nanostructural and micromagnetic parameters that lead to high  $H_c$  and  $\Phi_p$ . In Fig. 2e, the Spearman correlation coefficients of all parameters are presented on  $H_c$  and  $\Phi_p$ , respectively. Here  $\alpha$ , determining the reversal mechanism of magnetization to be either rotation or domain-wall motion, has the strongest effect on  $H_c$ , while moderate on  $\Phi_p$ . After  $\alpha$ ,  $L$  is the second strongest characteristic that inversely affects the  $H_c$ , in other words, higher  $L$  eventually leads to lower  $H_c$ . In addition to the diminishing pinning effect due to increased interval the decreasing volume fraction of 1:5-phase ( $\varphi_S \propto L^{-1}$ ) will also lead to a decrease in overall  $H_c$ , as it possesses the highest  $H_{\text{ani}}$  among three phases. Decreasing  $w_S$  can also lead to both diminishing pinning effect and reduced  $\varphi_S$ , but such correlation is the weakest among all the features. Meanwhile, properties of Z-phase have considerable effects on the inhomogeneity factor  $\Phi_p$ , among which  $w_Z$  has the strongest positive correlation while the domain-wall thickness  $l_{\text{dw}}^{(Z)}$  has the strongest negative one. Comparably, both  $L$  and  $w_S$  are less correlated to  $\Phi_p$ . Based on Spearman's correlations, the effects of the listed parameters can be hierarchically clustered as shown in Fig. 2g. The cluster arrangement indicates feature similarity, with branch point heights reflecting the degree of difference, i.e., greater height signifies greater dissimilarity. In this regard, it presents  $L$  and  $d$  as the most similar features, possibly because both quantities characterize the intervals between two platelet-shaped phases. The height of the branches connecting this cluster (orange) indicates the overall dissimilarity from the other two main clusters (green and red). It also demonstrates that effects of  $\alpha$  and  $M_s^{(Z)}$  are considerably similar, followed by  $w_Z$  and then  $w_S$ . The other two magnetic properties  $\sigma_{\text{dw}}^{(Z)}$  and  $l_{\text{dw}}^{(Z)}$ , however, belong to another cluster together with  $H_c$  and  $\Phi_p$ , suggesting that these two features are relatively close related to the coercivity and underlying pinning effects.

Permutation feature importance was also conducted to provide another perspective based on the calculation of increasing error of the prediction after permuting a feature randomly. As presented in Fig. 2f, the feature importance



highlights  $\alpha$  as the most influential feature for both  $H_c$  and  $\Phi_p$ . Following this, magnetic properties  $\sigma_{\text{dw}}^{(Z)}$  and  $M_s^{(Z)}$  present considerable importance on  $H_c$ , while the nanostructural parameters of Z-phase  $w_Z$  and  $d$  are important to  $\Phi_p$ . In comparison, nanostructural parameters of 1:5-phase, i.e.,  $L$  and  $w_S$ , are less important to both  $H_c$  and  $\Phi_p$ . Combining feature importance analyses based on correlation and permutation, the misorientation angle  $\alpha$  seems to be the most effective feature for both  $H_c$  and  $\Phi_p$ , implying that the grain structure of SmCo-1:7 permanent magnets exerts strong influences on the coercivity. Compared to the 1:5-phase, the Z-phase demonstrates more effective impedance to the domain wall motion (pinning effect), as  $\Phi_p$  is sensitive to its nanostructural and micromagnetic parameters. This is consistent with the physical perspective that the strong pinning effect of the Z-phase comes from its large disparity in  $\sigma_{\text{dw}}$  compared to other phases, indicating the extra energy fluctuation along with the domain wall motion across the Z-phase boundaries. On the other hand, the 1:5-phase has less effect on  $\Phi_p$ , but it still correlates with  $H_c$  considerably (mainly via  $L$ ), most likely due to its high intrinsic  $H_{\text{ani}}$ , which allows the 1:5-phase to influence the total  $H_c$  via its volume fraction.

Last but not least, we demonstrate the data-driven inverse design of SmCo-1:7 nanostructure from queried  $H_c$  and  $\Phi_p$ . In contrast to the  $f$ -NN model elaborated above, inverse design directly delivers the design parameters (nanostructural and micromagnetic parameters) for the specified target properties ( $H_c$  and  $\Phi_p$ ). This is different from the optimization task, which aims at extreme values of the properties while scanning the design spaces. Though also interesting, we leave it for the near future work. For the inverse design approach, another NN model, denoted by  $i$ -NN, was trained mapping  $H_c$  and  $\Phi_p$  onto the design parameters, as depicted in Fig. 1e. Note that it makes use of the forward  $f$ -NN model in the loss function of  $i$ -NN to improve the accuracy and avoid multiplicity of inverse predictions. Details are summarized in section *Method*. At the end,  $f$ -NN was also employed to cross-check the corresponding property value of the design parameters suggested by the inverse model.

In the following, we present a nanostructure inverse design case shown in Table. 1. Micromagnetic parameters are prescribed as  $\alpha = 0$  DFT-calculated  $M_s$ ,  $\sigma_{\text{dw}}$ , and  $l_{\text{dw}}$  (Supplementary Table 4), implying that the crystalline orientation and the magnetic properties of solid-state phases are known. Therefore, nanostructural parameters  $L$ ,  $d$ ,  $w_S$ , and  $w_Z$  are the sole output of the  $i$ -NN. Subsequent verifications are also carried out by importing the nanostructural parameters from inverse design into the  $f$ -NN model. In the presented three cases,  $H_c$  and  $\Phi_p$  of the inversely designed nanostructures have good agreement with the queries with the relative error below 5%. Notably, the first query ( $\mu_0 H_c^Q = 7$  T and  $\Phi_p^Q = 0.05$ ) gives a designed nanostructure with parameters outside the range of training dataset ( $L < 30$   $\mu\text{m}$ ), demonstrating a certain degree of extrapolative prediction. Nonetheless, the presented inverse design approach gains reasonable performance within a static range (minimum-maximum range as denoted by the boxplot in Fig. 2b) of queried properties. Specifically, queried properties that lie in the interquartile range can yield nanostructures with the least relative error. When the queried properties were in the outlier range, however, the  $i$ -NN model would sometimes output nanostructures with physically implausible parameters (like negative values). This again motivates us to extend the dataset with a larger range of nanostructural parameters or reduce the weights of outliers in future work.

To conclude this work, we integrate high-throughput micromagnetic simulation and machine learning approaches to investigate the influence of the cellular nanostructure on the coercivity of the SmCo-1:7 permanent magnets. After conducting data-driven forward analyses, we found:

- (i) Among nanostructural parameters,  $H_c$  is most sensitive to 1:5-phase interval  $L$ , while  $\Phi_p$  is most sensitive to  $w_Z$ . When the volume fraction of 1:5-phase  $\phi_S$  is sufficiently high, the tendency to increase  $H_c$  is dominated by increasing  $\phi_S$  rather than by decreasing  $\phi_Z$  (the volume fraction of Z-phase), while the highest  $\Phi_p$  still occurs when the nanostructure has 32%  $\sim$  42% Z-phase (around 5 at% Zr under the assumption of ideal lattice structure). These indicate that the Z-phase impedes the domain-wall motion more effectively, which aligns with the physical understanding of energy fluctuations during the domain-wall motion across adjacent phases. Nonetheless, increasing the amount of Z-phase eventually leads to a decrease in  $H_c$ , possibly attributing to its

comparably low  $H_{\text{ani}}$ . The role of 1:5-phase, on the other hand, is not only a provider of pinning sites but also a carrier of high  $H_{\text{ani}}$ . In this regard, tuning the 1:5-phase may be recognized as an elicited concern to achieve high coercivity in SmCo-1:7 magnets.

- (ii) Both  $H_c$  and  $\Phi_p$  are mostly sensitive to the misorientation angle  $\alpha$ . Meanwhile, pinning effects from the nanostructure have an evident contribution when misorientation exists ( $\alpha \neq 0$ ). These demonstrate the polycrystalline texture is still a factor that cannot be overlooked in optimizing the SmCo-1:7 microstructure for improving  $H_c$ , and the grains that have moderate misorientation ( $\alpha$  around  $30 \sim 60^\circ$ ) are the major beneficiary from the pinning effects.

Meanwhile, the presented work showcases the inverse design of nanostructural parameters by querying  $H_c$  and  $\Phi_p$  with acceptable precision. These ML-based models can readily find their applications in various synthesis and engineering situations as a computational cost-effective toolkit, for instance, the coercivity estimator and coercivity-based nanostructure predictor.

As a perspective, this work can be further conjugated with the scale-bridging hysteresis investigations, specifically, via connecting trained  $f$ -NN with vector hysteron on a mesoscopic polycrystal [40]. By incorporating dependencies of other alloying elements (like Cu and Fe), processing parameters (like the thermal history), and further properties (like the remanence) in the extended dataset, it is also promising to accelerate the design of novel SmCo-1:7 magnets with wide tailorable performances.

## Method

### First principle calculation of micromagnetic parameters

The magnetization saturation and exchange stiffness are evaluated combining the DFT calculation and the atomistic spin dynamics (ASD) simulation. Using the post-processing code 'jx' in OpenMx [41, 42] following a LDA + U self-consistent calculation [43], the exchange coupling parameters  $J_{ij}$  were calculated. In the self-consistent calculation, the magnitudes of U and J were selected as 6.7 and 0.7 eV, respectively, which are found to be suitable for most rare-earth elements. The energy cutoff and energy convergence criteria were set to 500 Ry and  $1.0 \times 10^{-8}$  Hartree, respectively.  $10 \times 10 \times 2$  and  $15 \times 15 \times 3$  k-meshes were used for self-consistent and  $J_{ij}$  calculations, respectively. By using the calculated exchange parameters and by assuming a continuous long-wavelength function for spin distribution in the Heisenberg Hamiltonian [44], the exchange stiffness of  $\text{Sm}(\text{Co}_{1.8}\text{Zr}_{0.4})_5$  was evaluated using the Uppsala Atomistic Spin Dynamics (UppASD) software [45]. The obtained magnetization saturation and exchange stiffness of  $\text{Sm}(\text{Co}_{1.8}\text{Zr}_{0.4})_5$  are 290 kA/m and 4.83 pJ/m, respectively.

### High-throughput micromagnetic simulation

The micromagnetic simulations were carried out by the FDM-based steepest conjugate gradient (SCG) solver in the open-sourced package MuMax<sup>3</sup> [46] with numerical details elaborated in Ref. [47]. Detailed theoretical essentials and simulation setups are documented in Supplementary Note 1 with the magnetic properties of each phase listed in Supplementary Table 4. More than 500 computational tasks were distributed in parallel onto computing nodes with the Nvidia<sup>®</sup> Volta 100 GPU. To balance the time consumption between computation and queuing, each distributed task batched 25-50 simulations and executed them in series. Processes, such as generation of nanostructures and inputfiles, job submission and management (incl. troubleshooting and subsequent inputfile correction/re-submission), and data collection as well as post-processing, were automated by customized Python scripts with utilities from multiprocessing library.

## Machine learning models for forward prediction

In this work, an ML-based forward prediction model for the micromagnetic simulation is essential to deal with data recursion and extrapolation, particularly in the permutation sensitivity test and contour surface extraction. Different ML models were trained using the nanostructural/magnetic parameters as the input and corresponding properties of interests (here the coercivity  $H_c$  and inhomogeneity factor  $\Phi_p$ ) from micromagnetic simulations as output, including the K-nearest neighbors, neural network, gradient boosting, decision tree, random forest, and support vector machine. These models were implemented in customized Python scripts with utilities from Scikit-learn and PyTorch library [48, 49]. Training of the forward models requires the minimization of the mean squared error (MSE) between the true values of properties ( $Y = \{H_c, \Phi_p\}$ ) and the prediction, i.e., the loss function is as

$$\mathcal{L} = \min_{\omega} \frac{1}{n} \sum \|\mathcal{F}_{\omega}[\mathbf{X}] - \mathbf{Y}\|^2, \quad (4)$$

where  $\mathcal{F}$  represents aforementioned ML models with a set of model parameters  $\omega$ ,  $\mathbf{X}$  stands for the nanostructural/magnetic parameters  $\mathbf{X} = \{L, d, w_S, w_Z, \alpha, M_s^{(Z)}, \sigma_{dw}^{(Z)}, l_{dw}^{(Z)}\}$ .

Model performance was evaluated by coefficient of determination ( $R^2$ ) and MSE between the true (from micromagnetic simulations) and the predicted (by forward prediction models) values. The selection of dataset size was examined in the sense of the weak law of large number (WLLN) and training performance, which are covered in Supplementary Note 2. The performance of the aforementioned six ML models was evaluated with their default hyperparameters, as presented in Supplementary Fig. 2 and 3. To improve the performance of the forward prediction models, which was practically employed in the subsequent data-driven analyses, hyperparameter optimization was also conducted with the performance presented in Supplementary Fig. 4. As the NN model was eventually employed in this work for forward prediction (i.e.,  $f$ -NN), the optimized hyperparameters are listed in Supplementary Table 3.

## Data-driven correlation and sensitivity analyses

To identify the most effective factors on the coercivity as well as the inhomogeneity factor, both correlation analysis and sensitivity analysis were performed in this work. Detailed theoretical essentials are documented in Supplementary Note 2.

We compared the Pearson’s correlation coefficient (a linear correlation) and Spearman’s correlation coefficient (a non-linear monotonic correlation), as shown in Supplementary Fig. 7, and eventually chose Spearman’s coefficient to present the correlation between properties of interest and the influencing factors. It is worth noting that Spearman’s correlation coefficient is defined in the range  $[-1, 1]$ , indicating the strength and direction of monotonic relationships between two quantities in a pair. Positive values signify direct correlations, while negative values indicate inverse correlations. Hierarchical clustering analysis was also conducted based on Spearman’s rank-order correlation.

Surrogate-based permutation importance test is employed for sensitivity analysis, where the importance of an influencing factor is calculated by quantifying the increase of the deviation in the prediction of the properties of interest after shuffling input values of the factors. An important feature is then the one with a largely increased error of prediction after the permutation. As the prerequisite, the  $f$ -NN model with optimized hyperparameters was trained for coercivity  $H_c$  and inhomogeneity factor  $\Phi_p$ .

## Machine learning model for inverse design

For inverse design, another NN model ( $i$ -NN) is employed to map the queried properties ( $Y = \{H_c, \Phi_p\}$ ) directly onto the design parameters (here  $\mathbf{X} = \{L, d, w_S, w_Z\}$  as micromagnetic parameters are prescribed). The main

challenge is to define a loss function that accurately identifies the correctness of a sole inversely-predicted  $\mathbf{X}$  while avoiding interference from multiple correct ones, as various nanostructures can result in a similar  $H_c$  and  $\Phi_p$ . To overcome this challenge, a modified loss function model is employed as [50]

$$\mathcal{L} = \min_{\nu} \frac{1}{n} \sum \left( \lambda \underbrace{\|\mathcal{I}_{\nu}[\mathbf{Y}] - \mathbf{X}\|^2}_{SE_i} + \underbrace{\|\mathcal{F}_{\omega}[\mathcal{I}_{\nu}[\mathbf{Y}]] - \mathbf{Y}\|^2}_{SE_f} \right) \quad \text{with } \lambda \geq 0, \quad (5)$$

where  $\mathcal{I}$  stands for the  $i$ -NN model with a set of model parameters  $\nu$ ,  $SE_i$  and  $SE_f$  are the squared errors of inverse prediction and forward verification, respectively. In this work, the forward verification ( $\mathcal{F}[\mathcal{I}[\mathbf{Y}]])$  is implemented by the  $f$ -NN model (details described in the section *Machine learning (ML) model for forward prediction*) rather than micromagnetic simulations. This strategy is also used in the other works of structural-parameter-based inverse design [50, 51]. The reason is not just for computational cost-efficiency, but also for performing automatic differentiation on loss function in the Adam optimizer in the training framework [52].  $\lambda$  is a regularization parameter for tuning the training performance, in this work  $\lambda = 0.02$ . It is worth noting the  $f$ -NN model remains the same as it used for forward data-driven analyses, but has  $\alpha$ ,  $M_s^{(Z)}$ ,  $\sigma_{dw}^{(Z)}$ , and  $l_{dw}^{(Z)}$  prescribed to fetch the  $i$ -NN outputs. The optimized hyperparameters are listed in Supplementary Table 3.

## Electron microscopy

Electron transparent specimens for TEM were fabricated by Ga focused ion beam (FIB) and plasma sputtering using dual beam SEM/FIB systems (Zeiss Crossbeam 540 and ThermoFisher Helios G4 plasma FIB). Bright-field (BF) TEM imaging and selected-area electron diffraction (SAED) measurements were carried in a conventional transmission electron microscope (JEOL JEM 2100F). High-resolution high angle annular dark field scanning TEM (HAADF-STEM) imaging was carried out in an aberration-corrected system (JEOL JEM-ARM200F) operated at 200 kV.

## Data Availability

The authors declare that the data supporting the findings of this study are available within the paper. The simulation results and utilities supplementary data and utilities are cured in the online dataset (DOI: [xx.xxxx/zenodo.xxxxxxx](https://doi.org/10.1101/2023.03.15.531111)).

## Acknowledgements

The authors acknowledge the financial support of German Science Foundation (DFG) in the framework of the Collaborative Research Centre Transregio 270 (CRC-TRR 270, project number 405553726, sub-projects A05, A06, A10, B13, Z01, Z-INF) and 361 (CRC-TRR 361, project number 492661287, sub-projects A05), and the Research Training Groups 2561 (GRK 2561, project number 413956820, sub-project A4). The authors also greatly appreciate the access to the Lichtenberg II High-Performance Computer (HPC) and the technique supports from the HHLR, Technische Universität Darmstadt, and the GPU Cluster from the CRC-TRR 270 sub-project Z-INF. The computing time on the HPC is granted by the NHR4CES Resource Allocation Board under the project "special00007". Y.Yang and M.Fathidoost highly thank Dr. Binbin Lin and Dr. Xiang-Long Peng for providing the strategy of training the forward and inverse ML models. Y.Yang and D.Ohmer also highly thank Prof. Michael Farle and Prof. Lambert Alff for intensive consultation and discussion.

## **Competing Interests**

The authors declare no competing financial or non-financial interests.

## **Author Contributions**

Conceptualization: B.-X.X. and Y.Y.; methodology: Y.Y., B.-X.X. and M.F.; software: Y.Y., and M.F.; characterization/validation: E.A. and L.M-L.; investigation: Y.Y., P.K. and E.F.; formal analysis: Y.Y., P.K. and M.F.; resources, K.S., O.G. R.X. and H.Z.; data curation, Y.Y.; writing—original draft preparation: Y.Y., P.K. and M.F.; writing—review and editing: all authors; visualization: Y.Y., M.F.; supervision, B.-X.X. and H.Z.; consultation and discussion: K.S. and O.G.; funding acquisition, K.S., H.Z., O.G., L M-L. and B.-X.X. All authors have read and agreed to the published version of the manuscript.



## References

- [1] Strnat, K. J. & Strnat, R. M. Rare earth-cobalt permanent magnets. *Journal of Magnetism and Magnetic Materials* **100**, 38–56 (1991).
- [2] Liu, J., Zhang, Y., Dimitrov, D. & Hadjipanayis, G. Microstructure and high temperature magnetic properties of sm (co, cu, fe, zr) z (z= 6.7–9.1) permanent magnets. *Journal of applied physics* **85**, 2800–2804 (1999).
- [3] Gutfleisch, O. *et al.* Evolution of magnetic domain structures and coercivity in high-performance smco 2:17-type permanent magnets. *Acta Materialia* **54**, 997–1008 (2006).
- [4] Katter, M., Weber, J., Assmus, W., Schrey, P. & Rodewald, W. A new model for the coercivity mechanism of sm/sub 2/(co, fe, cu, zr)/sub 17/magnets. *IEEE Transactions on Magnetics* **32**, 4815–4817 (1996).
- [5] Sepehri-Amin, H. *et al.* Correlation of microchemistry of cell boundary phase and interface structure to the coercivity of sm (co<sub>0.784</sub>fe<sub>0.100</sub>cu<sub>0.088</sub>zr<sub>0.028</sub>) 7.19 sintered magnets. *Acta Materialia* **126**, 1–10 (2017).
- [6] Giron, S. *et al.* Towards engineering the perfect defect in high-performing permanent magnets. *arXiv preprint arXiv:2304.14958* (2023).
- [7] Song, X., Liu, Y., Xiao, A., Yuan, T. & Ma, T. Cell-boundary-structure controlled magnetic-domain-wall-pinning in 2:17-type smcofeuzr permanent magnets. *Materials Characterization* **169**, 110575 (2020).
- [8] Duerrschnabel, M. *et al.* Atomic structure and domain wall pinning in samarium-cobalt-based permanent magnets. *Nature Communications* **8**, 7 Seiten (2022).
- [9] Kronmüller, H. & Goll, D. Analysis of the temperature dependence of the coercive field of sm<sub>2</sub>co<sub>17</sub> based magnets. *Scripta Materialia* **48**, 833–838 (2003).
- [10] Matthias, T. *et al.* TEM-analysis of sm(co,fe,cu,zr)z magnets for high-temperature applications. *Journal of Magnetism and Magnetic Materials* **242-245**, 1353–1355 (2002).
- [11] Pierobon, L. *et al.* Unconventional magnetization textures and domain-wall pinning in smco magnets. *Scientific Reports* **10** (2020).
- [12] Song, X. *et al.* Role of nanoscale interfacial defects on magnetic properties of the 2:17-type sm–co permanent magnets. *Journal of Alloys and Compounds* **816**, 152620 (2020).
- [13] Zhou, X. *et al.* Revisiting the pinning sites in 2:17-type sm-co-fe-cu-zr permanent magnets. *Journal of Rare Earths* **39**, 1560–1566 (2021). Special Issue of Multiscale Rare Earth Crystal Materials.
- [14] Tang, W., Zhang, Y. & Hadjipanayis, G. Effect of zr on the microstructure and magnetic properties of sm (cobalfe<sub>0.1</sub>cu<sub>0.088</sub>zrx) 8.5 magnets. *Journal of Applied Physics* **87**, 399–403 (2000).
- [15] Hadjipanayis, G. *et al.* High temperature 2:17 magnets: relationship of magnetic properties to microstructure and processing. *IEEE Transactions on Magnetics* **36**, 3382–3387 (2000).
- [16] Yan, A., Gutfleisch, O., Handstein, A., Gemming, T. & Müller, K.-H. Microstructure, microchemistry, and magnetic properties of melt-spun sm (co, fe, cu, zr) z magnets. *Journal of applied physics* **93**, 7975–7977 (2003).
- [17] Lectard, E., Allibert, C. & Ballou, R. Saturation magnetization and anisotropy fields in the sm (co<sub>1-x</sub>cux) 5 phases. *Journal of Applied Physics* **75**, 6277–6279 (1994).

- [18] Wang, Y. *et al.* Microstructure modification induced giant coercivity enhancement in sm(co,fe,cu,zr) permanent magnets. *Scripta Materialia* **146**, 231–235 (2018).
- [19] Maury, C., Rabenberg, L. & Allibert, C. H. Genesis of the cell microstructure in the sm(co,fe,cu,zr) permanent magnets with 2:17 type. *physica status solidi (a)* **140** (1993).
- [20] Yan, G. *et al.* Effect of grain boundary on magnetization behaviors in 2:17 type smco magnet. *Journal of Magnetism and Magnetic Materials* **489**, 165459 (2019).
- [21] Kronmüller, H. & Goll, D. Micromagnetic analysis of pinning-hardened nanostructured, nanocrystalline sm<sub>2</sub>co<sub>17</sub> based alloys. *Scripta Materialia* **47**, 545–550 (2002).
- [22] Gutfleisch, O. *et al.* Evolution of magnetic domain structures and coercivity in high-performance smco 2:17-type permanent magnets. *Acta Materialia* **54**, 997–1008 (2006).
- [23] Liu, J., Zhang, Y., Dimitrov, D. V. & Hadjipanayis, G. Microstructure and high temperature magnetic properties of sm(co,fe,cu,zr)<sub>z</sub> (z=6.7–9.1) permanent magnets. *Journal of Applied Physics* **85**, 2800–2804 (1999).
- [24] Zhang, Y. *et al.* Evolution of microstructure, microchemistry and coercivity in 2:17 type smco magnets with heat treatment. *IEEE Transactions on Magnetics* **37**, 2525–2527 (2001).
- [25] Zhang, C. *et al.* The evolution of phase constitution and microstructure in iron-rich 2:17-type sm-co magnets with high magnetic performance. *Scientific Reports* **8** (2018).
- [26] Matthias, T. *et al.* Tem-analysis of sm(co,fe,cu,zr)<sub>z</sub> magnets for high-temperature applications. *Journal of Magnetism and Magnetic Materials* **242-245**, 1353–1355 (2002). Proceedings of the Joint European Magnetic Symposia (JEMS'01).
- [27] Yan, A., Bollero, A., Gutfleisch, O., Müller, K.-H. & Schultz, L. Melt-spun precipitation hardened sm(co, fe, cu, zr)<sub>z</sub> magnets. *Materials Science and Engineering: A* **375-377**, 1169–1172 (2004).
- [28] Song, X. *et al.* Atomic scale understanding of the defects process in concurrent recrystallization and precipitation of sm-co-fe-cu-zr alloys. *Acta Materialia* **202**, 290–301 (2021).
- [29] Tang, W., Zhang, Y. & Hadjipanayis, G. C. Effect of zr on the microstructure and magnetic properties of sm(cobalfe<sub>0.1</sub>cu<sub>0.088</sub>zrx)<sub>8.5</sub> magnets. *Journal of Applied Physics* **87**, 399–403 (2000).
- [30] Jia, W. *et al.* Defects-aggregated cell boundaries induced domain wall curvature change in fe-rich sm(co,fe,cu,zr) permanent magnets. *Journal of Materials Science* **55**, 13258–13269 (2020).
- [31] Okabe, F. *et al.* Microstructures and magnetic domain structures of sintered sm(co 0.720fe<sub>0.200</sub>cu<sub>0.055</sub>zr<sub>0.025</sub>)<sub>7.5</sub> permanent magnet studied by transmission electron microscopy. *Materials Transactions* **47**, 218–223 (2006).
- [32] Wang, G. *et al.* Cellular structure regulation and coercivity enhancement induced by la<sub>2</sub>o<sub>3</sub> doping in 2:17 type smco magnet. *Journal of Alloys and Compounds* **849**, 156589 (2020).
- [33] Horiuchi, Y., Hagiwara, M., Endo, M., Sanada, N. & Sakurada, S. Influence of intermediate-heat treatment on the structure and magnetic properties of iron-rich sm(co,fe,cu,zr)<sub>z</sub> sintered magnets. *Journal of Applied Physics* **117**, 17C704 (2015).
- [34] Himanen, L., Geurts, A., Foster, A. S. & Rinke, P. Data-driven materials science: Status, challenges, and perspectives. *Advanced Science* **7**, 1903667 (2020).

- [35] Kronmuller, H., Kronmüller, H. *et al.* *Micromagnetism and the microstructure of ferromagnetic solids* (Cambridge university press, 2003).
- [36] Katter, M. *New rare-earth-iron based hard-magnetic materials* (na, 1991).
- [37] Yi, M., Gutfleisch, O. & Xu, B. X. Micromagnetic simulations on the grain shape effect in ndfeb magnets **120**.
- [38] Stoner, E. C. & Wohlfarth, E. A mechanism of magnetic hysteresis in heterogeneous alloys. *Philosophical Transactions of the Royal Society of London. Series A, Mathematical and Physical Sciences* **240**, 599–642 (1948).
- [39] Coey, J. M. *Magnetism And Magnetic Materials* (Cambridge university press, 2010).
- [40] Yang, Y., Kühn, P., Fathidoost, M. & Xu, B.-X. Micromagnetics and multiscale hysteresis simulations of permanent magnets. *COMPEL-The international journal for computation and mathematics in electrical and electronic engineering* **42**, 993–1006 (2023).
- [41] Terasawa, A., Matsumoto, M., Ozaki, T. & Gohda, Y. Efficient algorithm based on liechtenstein method for computing exchange coupling constants using localized basis set. *Journal of the Physical Society of Japan* **88**, 114706 (2019).
- [42] Ozaki, T. Variationally optimized atomic orbitals for large-scale electronic structures. *Physical Review B* **67**, 155108 (2003).
- [43] Anisimov, V. I., Aryasetiawan, F. & Lichtenstein, A. First-principles calculations of the electronic structure and spectra of strongly correlated systems: the lda+ u method. *Journal of Physics: Condensed Matter* **9**, 767 (1997).
- [44] Moreno, R. *et al.* Temperature-dependent exchange stiffness and domain wall width in co. *Physical review B* **94**, 104433 (2016).
- [45] Eriksson, O., Bergman, A., Bergqvist, L. & Hellsvik, J. *Atomistic spin dynamics: foundations and applications* (Oxford university press, 2017).
- [46] Vansteenkiste, A. *et al.* The design and verification of mumax3. *AIP Adv.* **4**, 107133 (2014).
- [47] Exl, L. *et al.* Labonte’s method revisited: An effective steepest descent method for micromagnetic energy minimization. *J. Appl. Phys.* **115**, 17D118 (2014).
- [48] Pedregosa, F. *et al.* Scikit-learn: Machine learning in python. *the Journal of machine Learning research* **12**, 2825–2830 (2011).
- [49] Paszke, A. *et al.* Pytorch: An imperative style, high-performance deep learning library. *Advances in neural information processing systems* **32** (2019).
- [50] Kumar, S., Tan, S., Zheng, L. & Kochmann, D. M. Inverse-designed spinodoid metamaterials. *npj Computational Materials* **6**, 73 (2020).
- [51] Peng, X.-L. & Xu, B.-X. Data-driven inverse design of composite triangular lattice structures. *International Journal of Mechanical Sciences* **265**, 108900 (2024).
- [52] Kingma, D. P. & Ba, J. Adam: A method for stochastic optimization. *arXiv preprint arXiv:1412.6980* (2014).

**Table 1.** Inverse design of nanostructural parameters with specified coercivity and inhomogeneity factor.

Queried Properties ( <i>i</i> -NN iutput)		Designed Nanostructural Parameters ( <i>i</i> -NN output)				Forward Cross-check ( <i>f</i> -NN output)		Reatlve Error (%)
$\mu_0 H_c^Q$ (T)	$\Phi_p^Q$	$L$ (nm)	$d$ (nm)	$w_S$ (nm)	$w_Z$ (nm)	$\mu_0 H_c^I$ (T)	$\Phi_p^I$	
7.0000	0.0500	10.5512	34.4364	7.2424	4.2517	7.0060	0.0488	0.0879
5.0000	0.0100	93.6572	21.5065	6.3650	9.6443	5.0007	0.0121	0.0446
4.0000	0.0000	120.7757	13.0958	6.5392	12.0948	4.149	0.0001	3.7317

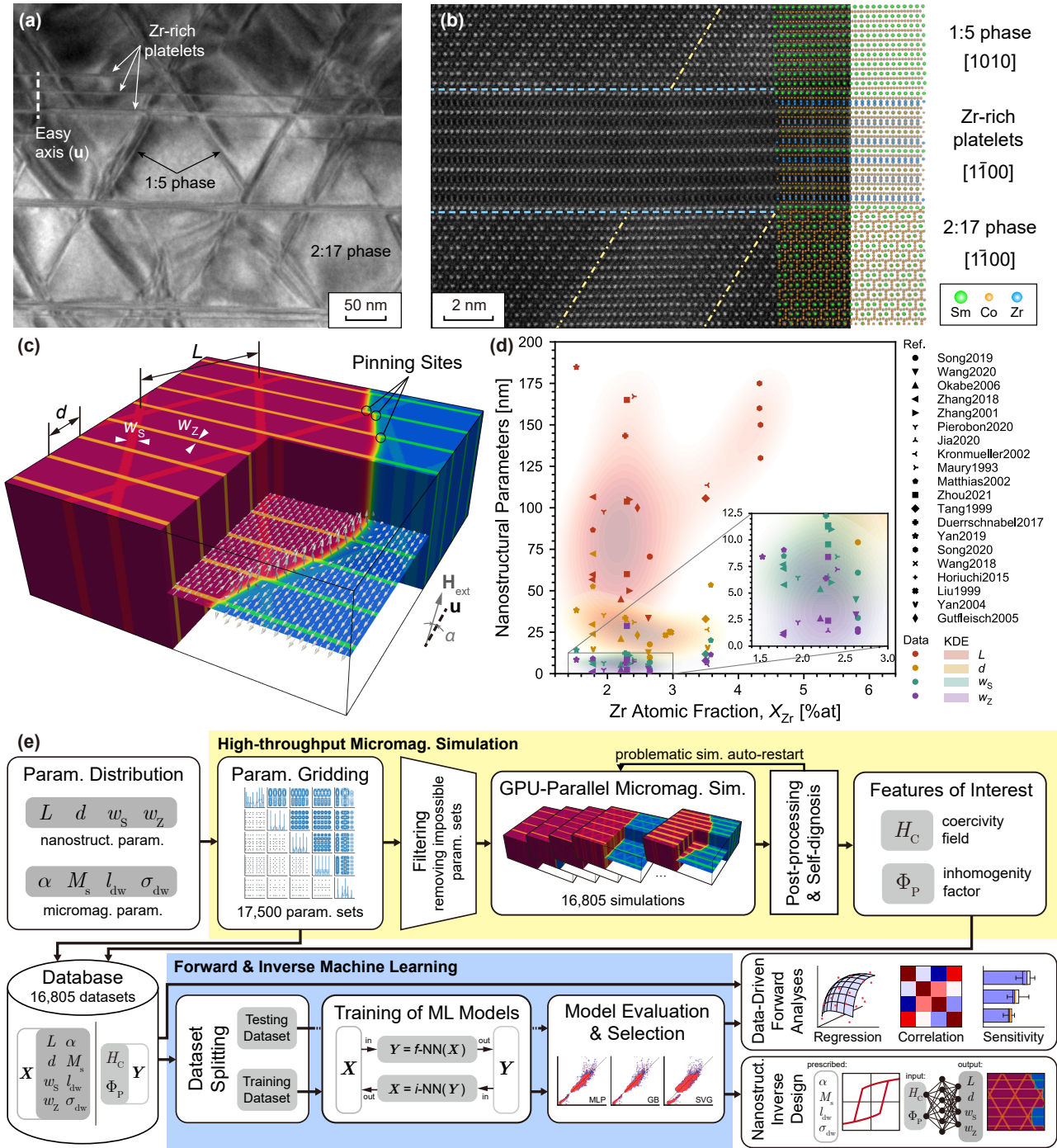


**Fig. 1. The nanostructure of the SmCo-1:7 magnets and the data-driven framework.** (a) Bright-field TEM image of the SmCo-1:7 magnets, where the nanostructure containing  $\text{Sm}(\text{Co,Cu})_5$ ,  $\text{Sm}_2(\text{Co,Fe})_{17}$  phases and Zr-rich platelet. (b) HAADF-STEM images of a local junction among phases, where the atomic stacking matches correspondingly the theoretical superlattice of each phase. (c) Domain structure from a micromagnetic simulation on parameterized nanostructure, where a  $180^\circ$  domain wall is pinned by pinning sites (phase junctions). (d) Distribution of the nanostructural parameters vs. atomic fracture of Zr ( $X_{Zr}$ ) from reviewed literatures [8, 11–13, 18–33]. (e) Data-driven framework combining high-throughput micromagnetic simulation and forward as well as inverse machine learning.



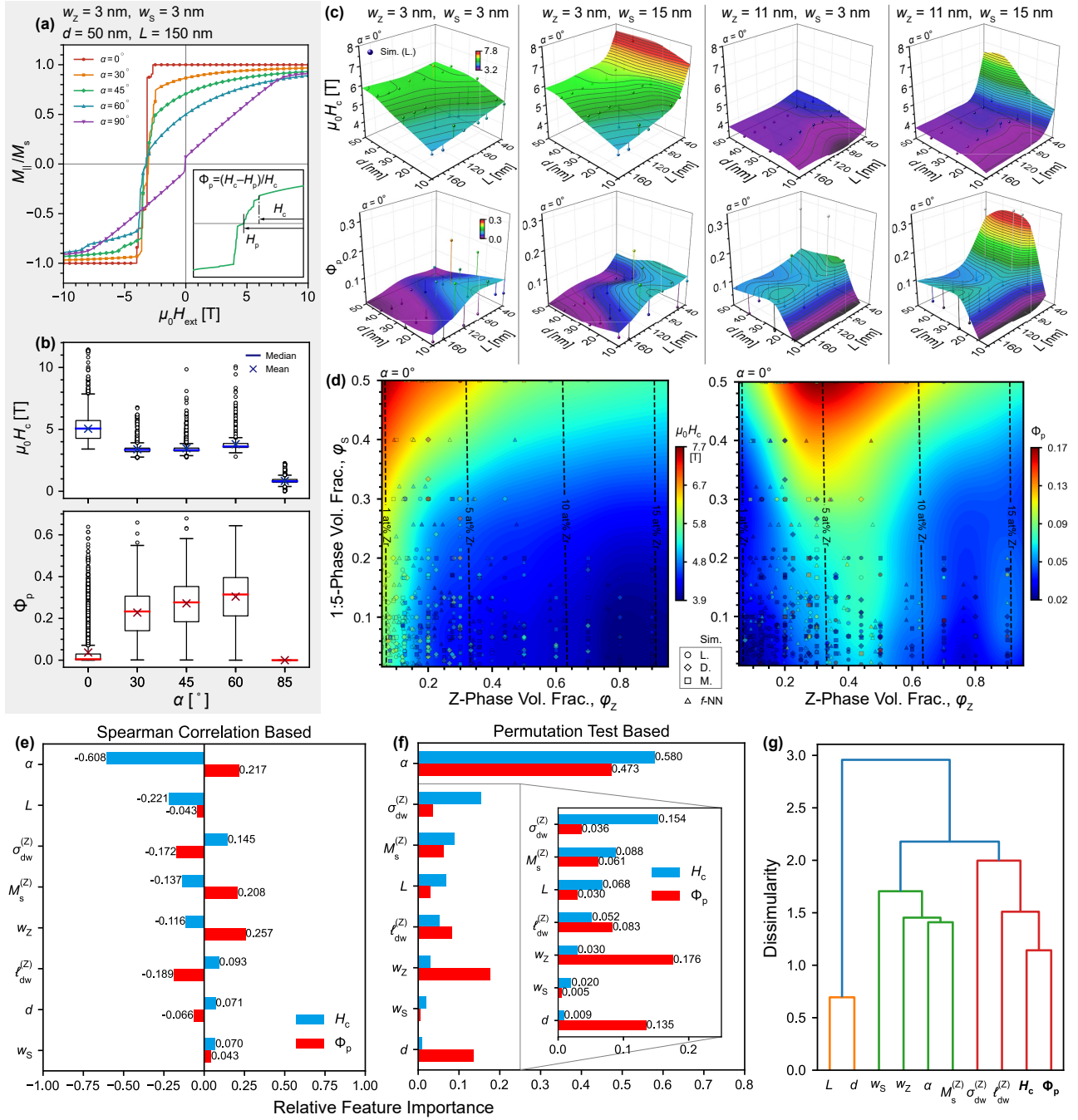


**Fig. 2. Data-driven analyses of the coercivity as well as the inhomogeneity factor in SmCo-1:7 nanostructures.** (a) Average half-cycle hysteresis of five demagnetizing processes by micromagnetic simulation for each misorientation angle  $\alpha$ . Here  $\mu_0$  is the vacuum permeability. Inset: quantification of the coercivity  $H_c$  and inhomogeneity factor  $\Phi_p = (H_c - H_p)/H_c$ . (b) Contour surfaces of  $H_c$  and  $\Phi_p$  vs. characteristic distances ( $L$  and  $d$ ) at various characteristic thicknesses of 1:5- and Z-phases ( $w_s$  and  $w_z$ ). (c) Boxplots of  $H_c$  and  $\Phi_p$  vs.  $\alpha$ , demonstrating their statistical angular dependency. (d) Contour surfaces of  $H_c$  and  $\Phi_p$  vs. volume fractions of corresponding phases  $\phi_s$  and  $\phi_z$ . Barplots of the relative feature importance of the nanostructural/magnetic parameters w.r.t.  $H_c$  and  $\Phi_p$  based on (e) Spearman correlation, and (f) permutation sensitivity test. (g) Hierarchical clustering diagram of the nanostructural/magnetic parameters together with  $H_c$  and  $\Phi_p$ .

# Supplementary Information

## Coercivity influence of nanostructure in SmCo-1:7 magnets: Machine learning of high-throughput micromagnetic data

Yangyiwei Yang<sup>a,\*</sup>, Patrick Kühn<sup>a</sup>, Mozhdeh Fathidoost<sup>a,\*</sup>, Esmaeil Adabifiroozjaei<sup>b</sup>, Ruiwen Xie<sup>c</sup>, Eren Foya<sup>a</sup>, Dominik Ohmer<sup>d</sup>, Konstantin Skokov<sup>e</sup>, Leopoldo Molina-Luna<sup>b</sup>, Oliver Gutfleisch<sup>e</sup>, Hongbin Zhang<sup>c</sup>, Bai-Xiang Xu<sup>a,\*</sup>

<sup>a</sup>Mechanics of Functional Materials Division, Institute of Materials Science, Technische Universität Darmstadt, Darmstadt 64287, Germany

<sup>b</sup>Advanced Electron Microscopy Division, Institute of Materials Science, Technische Universität Darmstadt, Darmstadt 64287, Germany

<sup>c</sup>Theory of Magnetic Materials Division, Institute of Materials Science, Technische Universität Darmstadt, Darmstadt 64287, Germany

<sup>d</sup>VACUUMSCHMELZE GmbH & Co. KG, 63450 Hanau, Germany

<sup>e</sup>Functional Materials (FM), Materials Science Department, Technical University of Darmstadt, Alarich-Weiss-Str. 16, 64287 Darmstadt, Germany

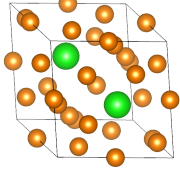
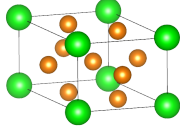
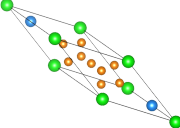
**Supplementary Table 1.** Nanostructural parameters of the Sm-Co permanent magnets from reviewed literature

Ref.	Sample	Prep.	Composition (at%)					Parameters (nm)			
			Sm	Co	Cu	Fe	Zr	$L$	$d$	$w_s$	$w_z$
[1]	Powder	Lab	11.905	58.583	5.286	22.024	2.202	-	-	-	-
[2]	Bulk	Lab	11.500	58.400	5.300	22.500	2.400	167.126	30.979	8.422	7.239
[3]	Powder	-	11.669	61.390	6.183	18.815	1.943	97.746	35.439	6.460	2.260
[4]	Powder	Lab	11.570	56.675	5.308	24.921	1.526	184.790	38.252	14.239	8.414
[5]	Powder	-	11.490	57.455	5.271	23.511	2.273	143.420	33.600	12.284	6.386
[6]	-	Lab	11.765	59.118	6.176	19.412	3.529	113.667	26.620	8.318	5.539
[7]	Powder	Lab & Industry	12.210	68.827	7.726	8.779	2.458	100.000	23.221	-	-
[8]	Bulk	Lab	12.500	56.263	7.000	21.350	2.888	-	23.203	-	-
			10.526	57.532	7.158	21.832	2.953	-	25.310	-	-
			9.901	57.934	7.208	21.984	2.973	-	24.876	-	-
[9]	Bulk	Lab	13.514	77.665	5.189	1.297	2.335	105.000	-	11.000	-
			13.514	77.665	5.189	1.297	2.335	50.000	-	6.000	-
[10]	Powder	Lab	11.038	57.559	4.715	24.909	1.779	106.538	72.284	5.777	-
			11.312	57.381	4.700	24.833	1.774	59.758	23.939	7.306	1.275
			11.628	57.177	4.684	24.744	1.767	56.736	29.724	7.684	1.065
[11]	Powder	Lab	11.111	67.911	6.756	12.444	1.778	86.636	52.614	8.489	9.060
			9.622	62.638	11.633	12.528	3.579	-	53.453	20.124	11.473
[12]	Ribbon	Lab	11.732	65.978	7.133	13.374	1.783	-	14.661	-	-
			11.765	65.294	10.588	8.824	3.529	-	15.664	-	-
[13]	Powder	Lab	11.748	60.185	3.234	20.496	4.337	130.000	-	-	-
			11.748	60.185	3.234	20.496	4.337	150.000	-	-	-
			11.707	53.642	3.222	27.106	4.322	160.000	-	-	-
			11.707	53.642	3.222	27.106	4.322	175.000	-	-	-
[14]	Powder	Lab	11.765	60.000	6.176	19.412	2.647	70.571	17.692	2.662	1.353
			11.765	60.000	6.176	19.412	2.647	-	9.783	6.918	1.596
[15]	Powder	Lab	12.500	67.550	7.700	8.750	3.500	105.719	32.956	11.834	7.832
[16]	Foil	Lab	11.601	50.786	5.961	29.358	2.294	-	-	-	-
			11.616	53.223	5.968	26.895	2.297	-	31.952	6.574	1.443
[17]	Powder	Lab	11.765	63.529	4.853	17.647	2.206	-	-	-	-
[18]	Powder	Lab	12.500	69.125	7.875	7.875	2.625	33.597	12.906	4.414	2.984
[19]	Powder	Lab	11.616	53.223	5.968	26.895	2.297	60.016	-	11.268	28.800
			11.616	53.223	5.968	26.895	2.297	165.023	-	11.372	8.400
			11.616	53.223	5.968	26.895	2.297	103.756	-	9.585	2.400
[20]	Powder	-	11.364	50.700	5.318	31.023	1.595	-	-	-	-

\*Corresponding author

Email addresses: yangyiwei.yang@mfm.tu-darmstadt.de (Yangyiwei Yang), mozhdeh.fathidoost@mfm.tu-darmstadt.de (Mozhdeh Fathidoost), xu@mfm.tu-darmstadt.de (Bai-Xiang Xu)

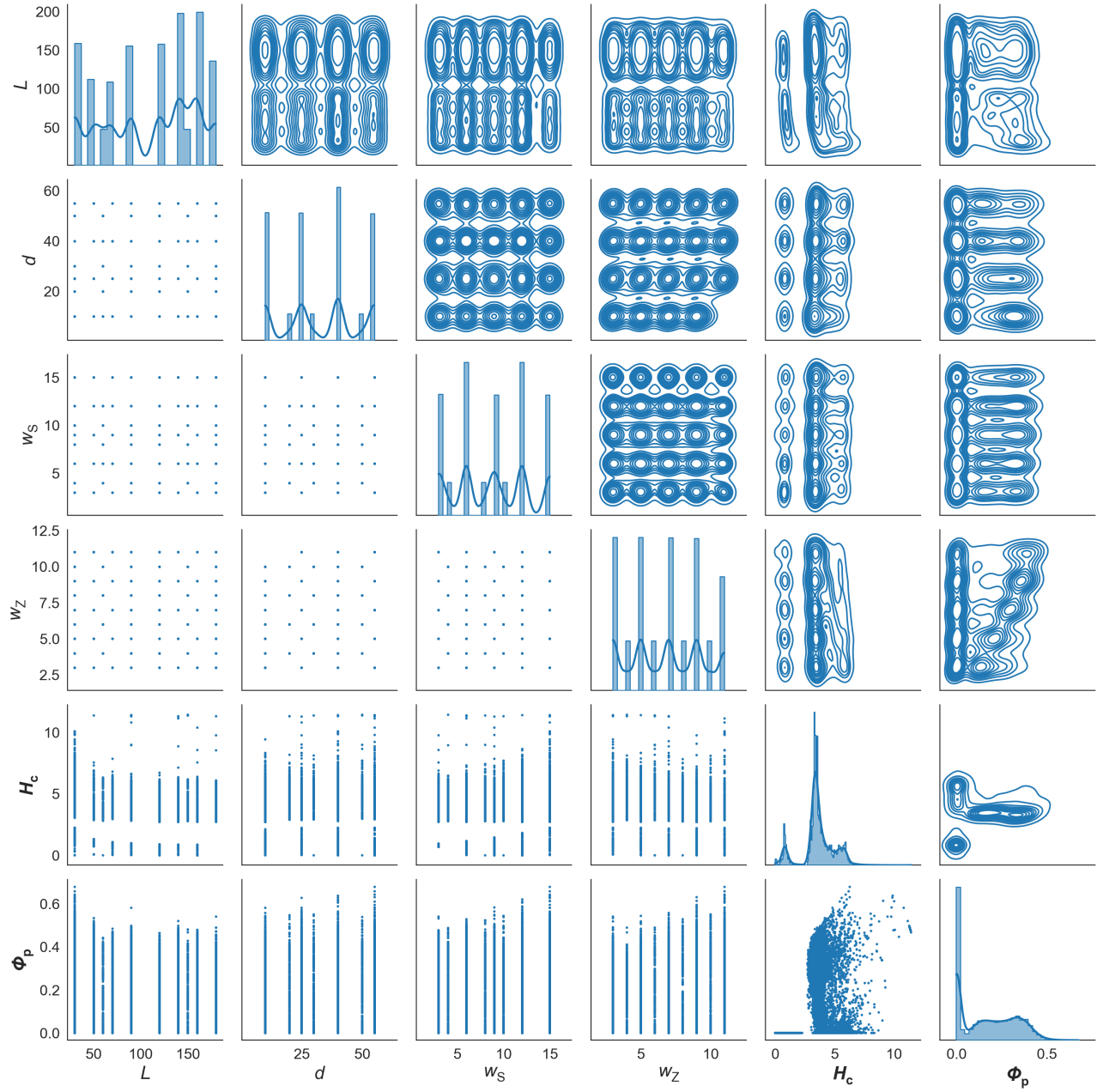
**Supplementary Table 2.** Unit cell (UC) structures of nanoscopic phases and their descriptors.

Phase	Unit Cell	Space Group	UC Composition	UC Volume ( $\text{\AA}^3$ )
2:17 (C)		$R\bar{3}m$	$\text{Sm}_2\text{Co}_{17}$	248.297
1:5 (S)		$P6/mmm$	$\text{SmCo}_5$	89.138
Zr-rich (Z)		$R\bar{3}m$	$\text{Sm}(\text{Co}_{1.8}\text{Zr}_{0.4})_5$	181.968

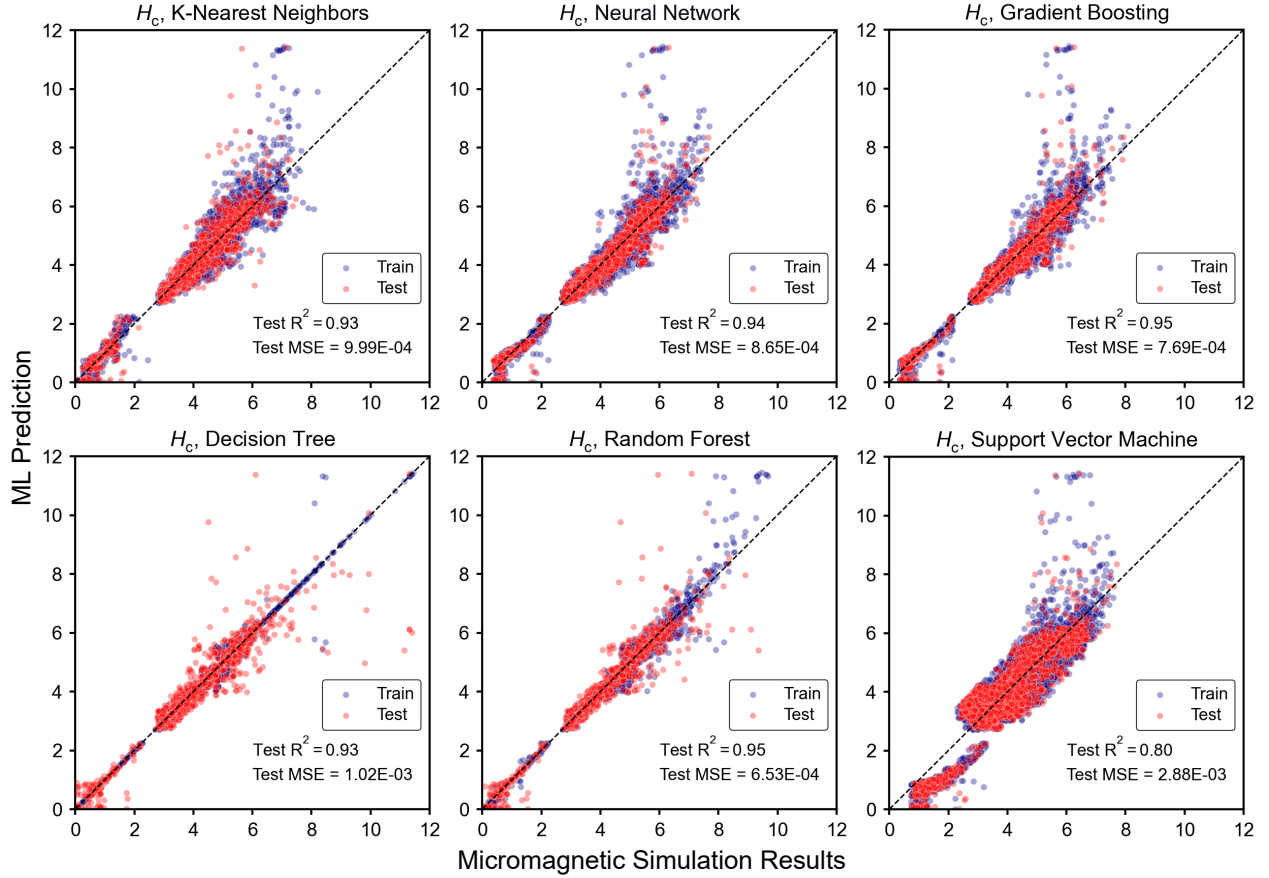
The atomic fraction  $f_a^A$  of an element  $A$  is then calculated by

$$f_a^A = \frac{\sum_p \phi^p r_p^A N_{\text{uc}}^p / V_{\text{uc}}^p}{\sum_p \phi^p N_{\text{uc}}^p / V_{\text{uc}}^p}, \quad (1)$$

where  $f_v^p$  are the volume fraction of the phase  $p$ ,  $r_p^A$  is the atomic ratio of the element  $A$  in a unit cell (UC),  $N_{\text{uc}}^p$  and  $V_{\text{uc}}^p$  are the number of UCs and the corresponding volume for the phase  $p$ . Taking a single UC, i.e.,  $N_{\text{uc}}^p = 1$ ,  $V_{\text{uc}}^p$  then represents the UC volume, as listed in Supplementary Table 2.

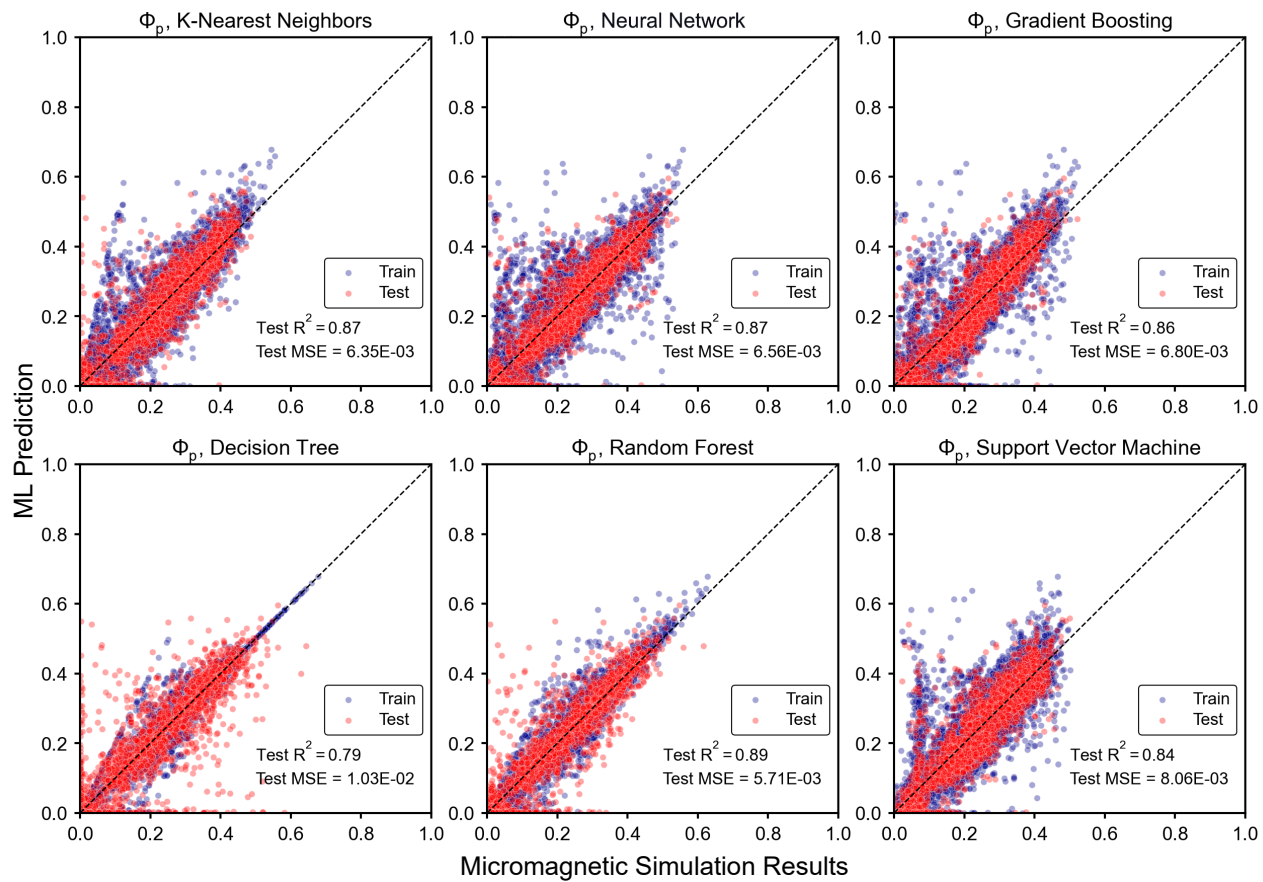


**Supplementary Fig. 1.** Pairplot of the sampled nanostructural parameters with the corresponding  $H_c$  and  $\Phi_p$ , where the lower-left sub-figures present the distribution, the diagonal ones present the statistics, and the upper-right ones present the kernel density estimate (KDE).



**Supplementary Fig. 2.** Scatter plots of the coercive field  $H_c$  values predicted by machine learning models versus the micromagnetic simulation results. As performance scores, the coefficient of determination ( $R^2$ ) and mean squared error (MSE) are correspondingly calculated as  $R^2 = \frac{\sum_i (\hat{y}_i - \bar{y})^2}{\sum_i (y_i - \bar{y})^2}$ , and  $MSE = \frac{1}{N} \sum_i (y_i - \hat{y}_i)^2$ ,  $N$ ,  $y_i$ ,  $\hat{y}_i$  and  $\bar{y}$  represent the size of the dataset, the true value, the predicted value and the mean of the dataset, respectively.





**Supplementary Fig. 3.** Scatter plots of the pinning contribution fraction  $\Phi_p$  values predicted by machine learning models versus the micromagnetic simulation results.

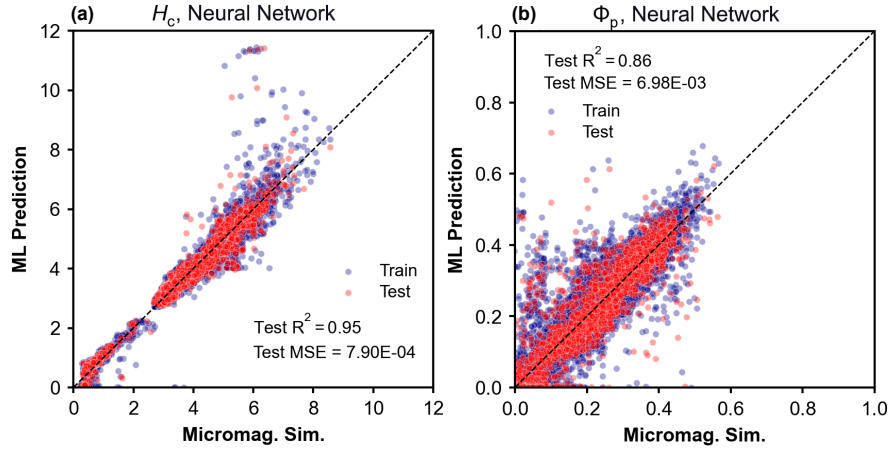
**Supplementary Table 3.** Optimized hyperparameters for the forward ( $f$ -NN) and inverse neural network ( $i$ -NN).

	$f$ -NN	$i$ -NN
Batch size	128	128
Input, (hidden), output layers	$8^*$ , (64, 64), 2	2, (128, 128), 4
Activation function	ReLU	ReLU
Optimizer	Adam	Adam
Learning rate	0.001	0.001
Epochs (stop/total)	247/2000	100/100**
Numerical scaling	$\mu \pm \sigma \rightarrow \pm 1$ ***	$\mu \pm \sigma \rightarrow \pm 1$

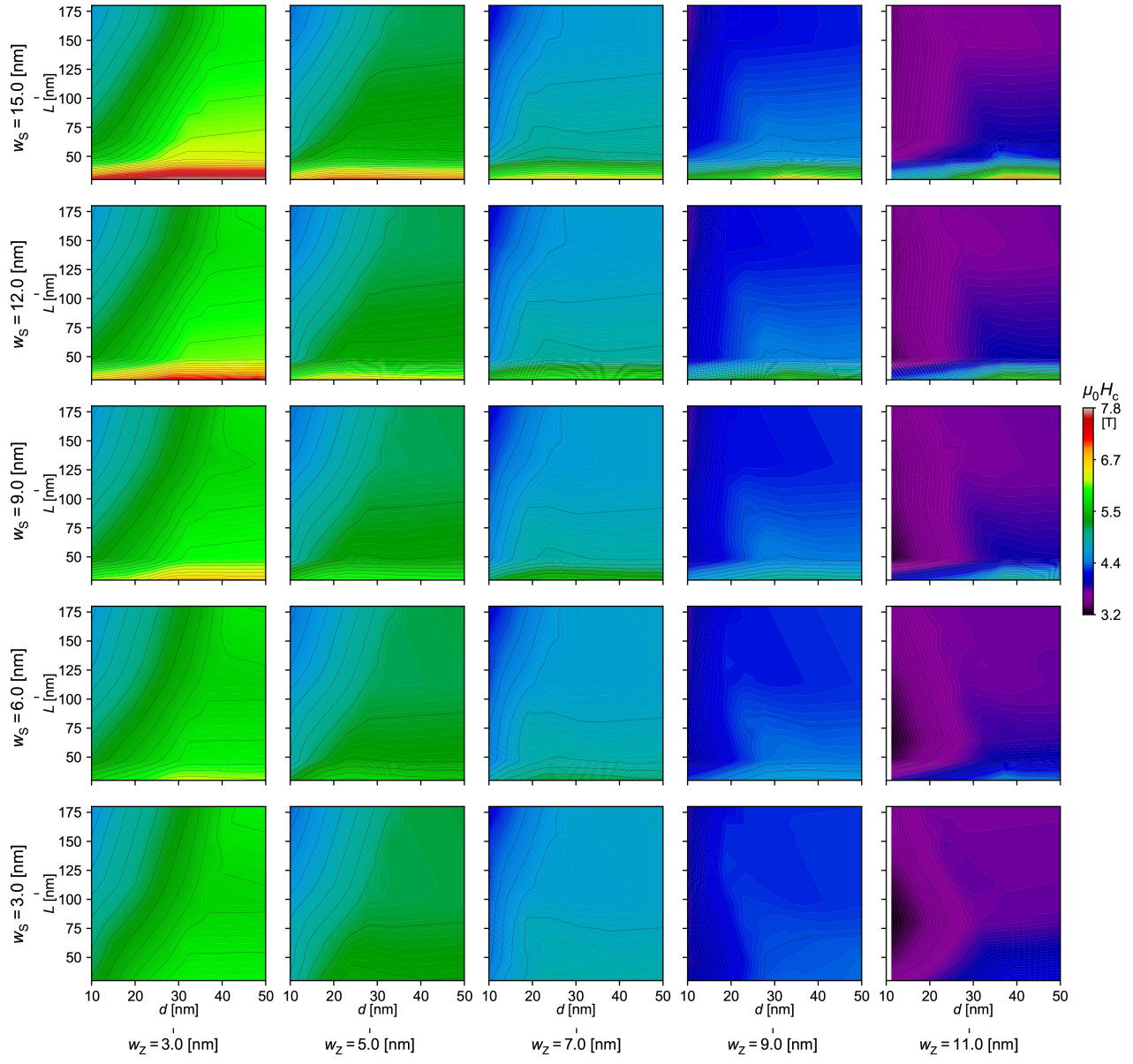
\* When training of the  $i$ -NN model, four of the eight inputs, i.e.,  $\alpha$ ,  $M_s^{(Z)}$ ,  $\sigma_{dw}^{(Z)}$  and  $I_{dw}^{(Z)}$ , are prescribed with constant values.

\*\* The  $i$ -NN is curated after each epoch, and the one with minimum test loss is selected as final model.

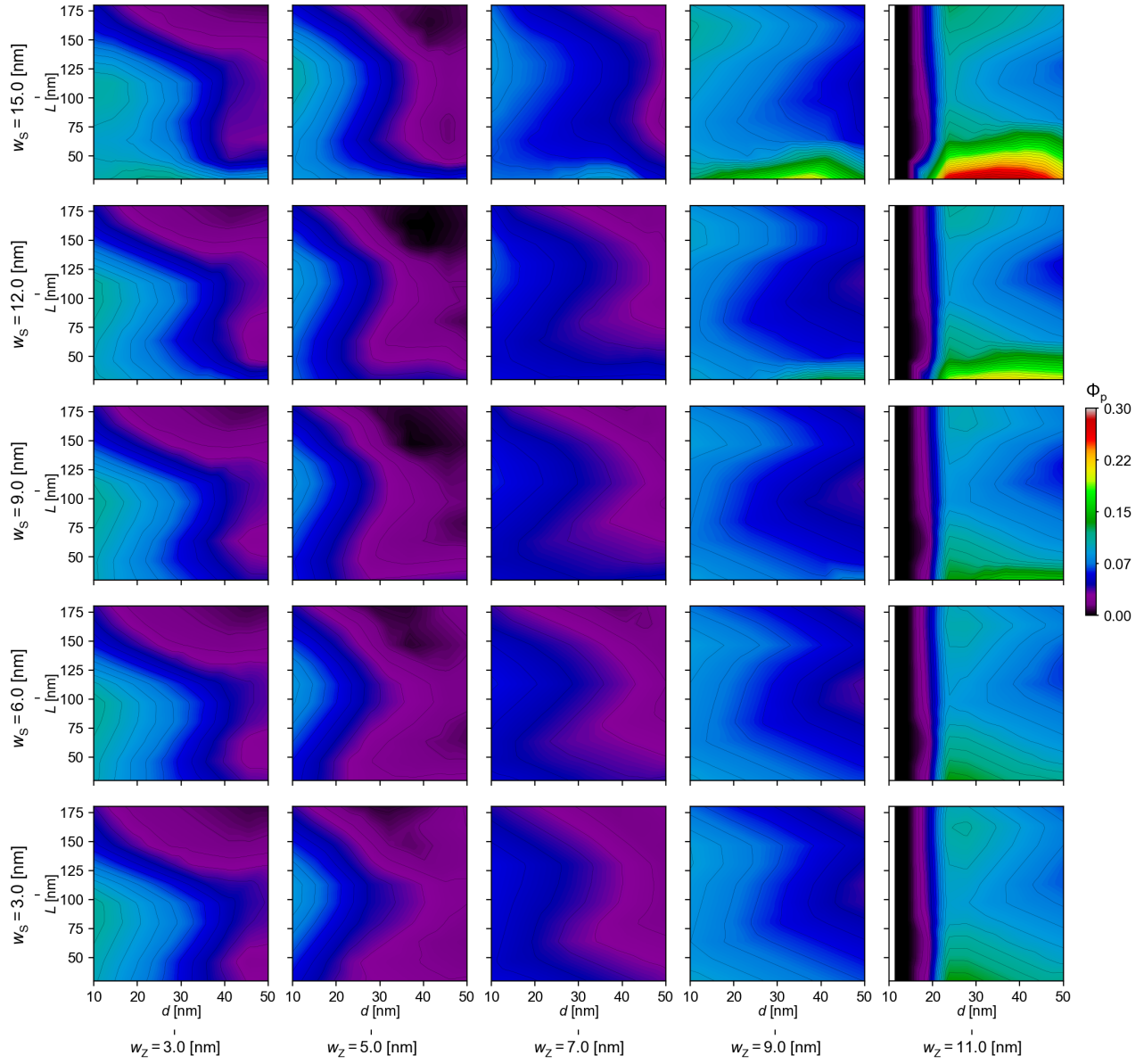
\*\*\* Here  $\mu$  stands for the mean and  $\sigma$  stands for standard deviation.



**Supplementary Fig. 4.** Scatter plots of (a) the coercive field  $H_c$  and (b) the pinning contribution fraction  $\Phi_p$  values, predicted by  $f$ -NN model after the hyperparameter optimization versus the micromagnetic simulation results.



**Supplementary Fig. 5.**  $H_c$  contours with varying nanostructural parameters ( $L$ ,  $d$ ,  $w_S$ ,  $w_Z$ ). The misorientation angle  $\alpha = 0^\circ$ .



**Supplementary Fig. 6.**  $\Phi_p$  contours with varying nanostructural parameters ( $L, d, w_s, w_z$ ). The misorientation angle  $\alpha = 0^\circ$ .

## Supplementary Note 1. Micromagnetic simulation

### 1.1. Theoretical formulations

In micromagnetics, magnetization is treated as a position-dependent vector  $\mathbf{m}(\mathbf{r})$ , normalized with respect to the saturation magnetization, i.e.,  $\mathbf{m} = \mathbf{M}/M_s$ . Physically, this can be interpreted as the mean field of local magnetic moments. In order to model the magnetization reversal within a micromagnetic system the free energy is formulated as a functional of  $\mathbf{m}(\mathbf{r})$  as

$$\mathcal{F} = \int_V [f_{\text{ex}} + f_{\text{ani}} + f_{\text{ms}} + f_{\text{zm}}] dV, \quad (2)$$

where the separate contributions  $f_{\text{ex}}$ ,  $f_{\text{ani}}$ ,  $f_{\text{ms}}$  and  $f_{\text{zm}}$  represent contributions from exchange, magneto-crystalline anisotropy, magnetostatics and external magnetic field, respectively. They are formulated as

$$\begin{aligned} f_{\text{ex}} &= A_{\text{ex}} \|\nabla \mathbf{m}\|^2, \\ f_{\text{ani}} &= - \sum_i K_{\text{u}} (\mathbf{u} \cdot \mathbf{m})^{2i}, \\ f_{\text{ms}} &= - \frac{1}{2} \mu_0 M_s \mathbf{m} \cdot \mathbf{H}_{\text{dm}}, \\ f_{\text{zm}} &= - \mu_0 M_s \mathbf{m} \cdot \mathbf{H}. \end{aligned} \quad (3)$$

The exchange energy  $f_{\text{ex}}$  recapitulates the tendency of neighboring magnetic moments to align parallel due to Heisenberg exchange interaction, therefore it can be interpreted as a local driving force of domain wall migration, for this calculation a positive exchange parameter  $A_{\text{ex}}$  is required.  $f_{\text{ani}}$  the contribution from magneto-crystalline anisotropy takes into account the orientation of the system, this is related to the easy axis  $\mathbf{u}$  (normally the principal axis). The parameter  $K_{\text{u}i}$  is the anisotropy constant, commonly only its lowest order is employed. In SI units  $K_{\text{u}}$  and  $A_{\text{ex}}$  can directly be related to the exchange length  $l_{\text{dw}}$  and domain wall energy  $\sigma_{\text{dw}}$  via

$$\sigma_{\text{dw}} = 4\sqrt{A_{\text{ex}}K_{\text{u}}} \quad \text{and} \quad l_{\text{dw}} = \pi\sqrt{\frac{A_{\text{ex}}}{K_{\text{u}}}}, \quad (4)$$

Other than the material-dependent terms  $f_{\text{ex}}$  and  $f_{\text{ani}}$ ,  $f_{\text{ms}}$  and  $f_{\text{zm}}$  take into account the interaction among magnetization and interaction with magnetic extrinsic magnetic fields. In particular  $f_{\text{ms}}$  counts the energy of each local magnetization under the demagnetizing field created by surrounding magnetization, it should be noted that the demagnetizing field  $\mathbf{H}_{\text{dm}}$  highly depends on the boundary conditions applied. The Zeemann term  $f_{\text{zm}}$  accounts for the energy of each local magnetization under the external applied field. Supplementary Table 4 provides a summary of all micromagnetic parameters used in this work.

Evolution of the magnetization configuration  $\mathbf{m}(\mathbf{r})$  under a cycling  $\mathbf{H}_{\text{ext}}$  was generally described by the Landau-Lifshitz-Gilbert equation, which is mathematically formulated as

$$\frac{\partial \mathbf{m}}{\partial t} = \frac{\gamma_{\text{mg}}}{1 + \alpha_{\text{d}}^2} \frac{1}{\mu_0 M_s} \left[ \mathbf{m} \times \frac{\delta \mathcal{F}}{\delta \mathbf{m}} + \alpha_{\text{d}} \mathbf{m} \times \left( \mathbf{m} \times \frac{\delta \mathcal{F}}{\delta \mathbf{m}} \right) \right], \quad (5)$$

with the vacuum permeability  $\mu_0$ , the gyromagnetic ratio  $\gamma_{\text{mg}}$  and the damping coefficient  $\alpha_{\text{d}}$ . However, due to the incomparable time scale of LLG-described magnetization dynamics (around nanoseconds) with respect to the one of hysteresis measurement (around seconds), constrained optimization of the free energy functional  $\mathcal{F}$  has been widely employed as a computationally efficient alternative to the time-dependent calculation in evaluating the hysteresis behavior of permanent magnets [21–23]. Based on the steepest conjugate gradient (SCG) method, the iteration scheme is derived as

$$\begin{aligned} \frac{\mathbf{m}^{(i+1)} - \mathbf{m}^{(i)}}{\Delta^{(i)}} &= \mathbf{m}^{(i)} \times \frac{1}{\mu_0 M_s} \left[ \mathbf{m}^{(i)} \times \frac{\delta \mathcal{F}}{\delta \mathbf{m}^{(i)}} \right], \\ \text{subject to} \quad |\mathbf{m}| &= 1 \end{aligned} \quad (6)$$

with the iteration step size  $\Delta^{(i)}$  and the magnetization configuration  $\mathbf{m}^{(i)}$  of the step  $i$ . The iteration scheme in Eq. (6) is in accordance with the sole damping term of the LLG equation (Eq. (5)) [21, 23]. This also means that the magnetic hysteresis is evaluated under the quasi-static condition.



**Supplementary Table 4.** Micromagnetic parameters for the phases appearing in this work.

Quantities	Unit	Sm <sub>2</sub> Co <sub>17</sub>	SmCo <sub>5</sub>	Zr-rich		
				Lit.	DFT	Mod.
$A_{\text{ex}}$	$\text{pJ m}^{-1}$	19.60	8.60	0.48	4.83	0.70
$K_{\text{u}}$	$\text{MJ m}^{-3}$	3.9	18.3	2.1	2.1	1.4
$M_{\text{sat}}$	$\text{kA m}^{-1}$	987.7	810.8	310.4	290.0	310.4
$l_{\text{dw}}$	nm	7.0	2.2	1.5	4.8	2.2
$\sigma_{\text{dw}}$	$\text{mJ m}^{-2}$	35.0	50.2	4.0	12.7	4.0

## 1.2. Simulation setup

To simulate the behavior of Sm-Co, a parameterized nanostructure is used, following the work of Katter et al.[24], which has been collectively introduced in the main text. Two different finite difference domains, i.e. the small domain  $128 \times 128 \times 32 \text{ nm}^3$  and the large domain  $192 \times 192 \times 32 \text{ nm}^3$ , are used in the implementation of micromagnetic simulations with a grid size  $0.5 \times 0.5 \times 2 \text{ nm}^3$ . Here, the small domain is used mainly for nanostructures with relatively small  $L$  parameters ( $L < 140 \text{ nm}$ ) under the consideration of improving computational efficiency. We use the large domain not only to resolve complete nanostructures with relatively large  $L$  parameters ( $L \geq 140 \text{ nm}$ ), but also to reconstruct several nanostructures with  $L < 140 \text{ nm}$  for double-checking. In this regard, 7,137 simulations out of in total 17,500 are carried out on the large simulation domain.

Different boundary conditions (BCs) are applied on different domain boundaries of the simulation domain. Periodic boundary condition (PBC) is applied along the out-of-plane ( $z$ ) direction by macro geometry approach [25] whereas all other faces are subject to Neumann BC [26]. Since the in-plane domain configuration and domain wall migration are mainly resolved. In that sense, the grid number along the out-of-plane direction was decreased for the reduction of computational consumption. Meanwhile, to emulate the effects of grain boundary in reducing the nucleation field, a grain boundary layer of 2 nm is introduced. This layer is assumed to have eliminated  $K_{\text{u}}$  but identical  $A_{\text{ex}}$  and  $M_{\text{s}}$  as 2:17-phase.

It is worth noting that the magnetic exchange coupling on the interface inherently differs from the bulk phases, determined by the local structure and chemical component. Such difference further influence the domain wall migration across interfaces. Here we adopt the interface effective field from Ref. [26] as

$$\mathbf{H}_{\text{ex}}^{\text{intf}} = \frac{2S}{\mu_0} \langle A_{\text{ex}}/M_{\text{s}} \rangle_{\text{H}} \nabla \cdot \nabla \mathbf{m}, \quad (7)$$

where  $\langle A_{\text{ex}}/M_{\text{s}} \rangle_{\text{H}}$  represents the harmonic mean of  $A_{\text{ex}}/M_{\text{s}}$  of adjacent bulk phases, and  $S$  is a strength factor. It has been shown that the reduced  $S$  from one brings extra pinning effects onto the domain wall migration [27], as  $S = 1$  can be physically interpreted as a complete atomic contact across the interface [28]. To avoid complexity in the analyses, in this work, we take the default  $S = 1$  for the interfaces among all solid-state phases with the assumption of complete atomic contacts, based on the observation of coherent atomic stacks. The interface between phases and grain boundary layer is also assumed to have  $S = 1$ .

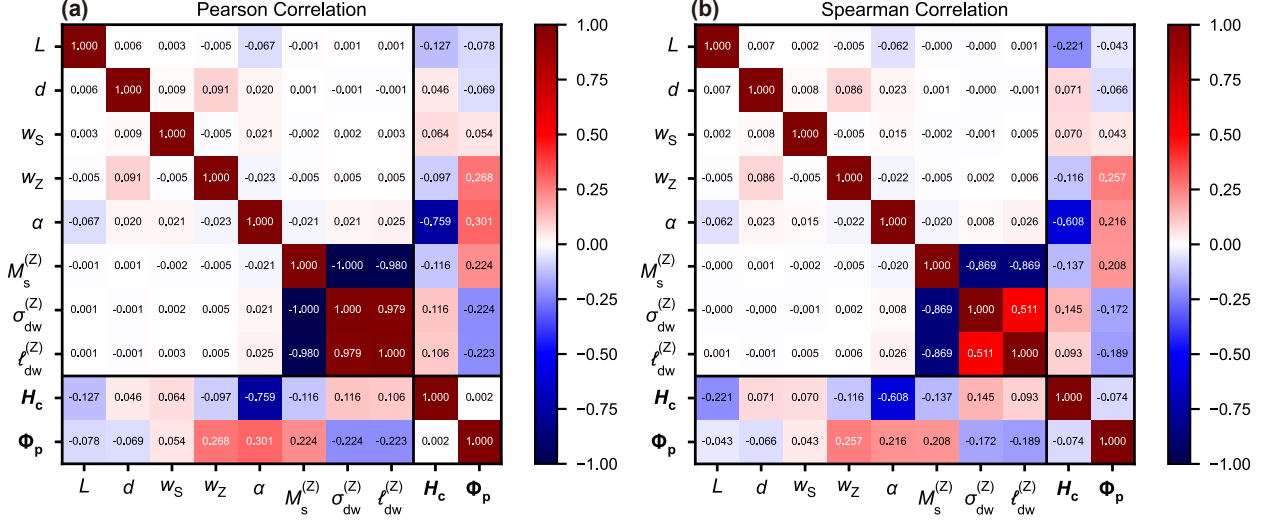
## Supplementary Note 2. Data-driven analyses

### 2.1. Sensitivity analysis

Sensitivity analysis is a technique utilized in data-driven analysis to measure the uncertainties in model parameters. It evaluates the impact of changes in models, methods, and variable values on the final output, and therefore, it is a valuable tool in designing materials with specific properties. SA identifies the input variables that have the most significant influence on the outcome, making it a powerful tool for this purpose. To apply data-driven and machine-learning techniques effectively, it is essential to have a complete and extensive dataset, which can be obtained from experiments or simulations [29–32].

### 2.2. Correlation analysis

The significance of characteristics is determined via correlation analysis. In this work, we compared the results of Pearson and Spearman correlations:



Supplementary Fig. 7. Heatmaps of Pearson's and Spearman's correlation.

### (1) Pearson Correlation

The Pearson Correlation is calculated as

$$R_{X,Y} = \frac{\text{cov}(X,Y)}{\sigma_X \sigma_Y}, \quad (8)$$

where, the input and output vectors are represented by  $\mathbf{X} = [x_1, x_2, \dots, x_i]$  and  $\mathbf{Y} = [y_1, y_2, \dots, y_i]$  respectively, while  $\text{cov}(\cdot)$  is the covariance operator, and  $\sigma_X$  and  $\sigma_Y$  are the standard deviation of  $\mathbf{X}$  and  $\mathbf{Y}$  respectively. A correlation coefficient of minus one indicates a perfect negative linear correlation between two variables, while a value of zero implies no linear relationship between the two variables. A correlation coefficient of one indicates a complete positive linear correlation between two variables. The magnitude of the correlation coefficient indicates the strength of the correlation between the two variables; the larger the coefficient, the stronger the correlation [29, 30].

### (2) Spearman Correlation

Spearman's Correlation is often described as Pearson's correlation coefficient applied to ranked variables. While Pearson's correlation focuses on linear relationships between variables, Spearman's correlation looks at how well the relationship between two variables can be described with a monotonic function [33]. The Spearman's rank coefficient, denoted as  $\rho$ , is calculated using the formula

$$\rho = 1 - \frac{6 \sum d_i^2}{n(n^2 - 1)} \quad (9)$$

Here,  $\rho$  represents the Spearman's rank correlation,  $d_i$  stands for the difference of ranks of observations, and  $n$  denotes the number of observations.

In this work, we measured both the Pearson's and Spearman's correlations and the results are shown in Supplementary Fig. 7 a and b, respectively. The two methods yield slightly varied correlations between the quantities. Pearson's analysis implies a close to perfect correlation between  $\sigma_{dw}$  and  $L$ , whereas the Spearman correlation indicates only about half of this strength. Additionally, the Spearman's correlation for  $\Phi_p$  of all quantities is less pronounced compared to the Pearson's correlation. For  $H_c$ , the results are more mixed, but in most cases, the Spearman correlation is stronger than the Pearson correlation.

In summary, selecting the type of measuring correlation is a crucial step in determining the relationship between variables. Pearson's correlation coefficient is a parametric measure indicating a linear relationship between variables. Spearman's correlation coefficient, on the other hand, is non-parametric, computed based on ranks, and illustrates both linear and non-linear monotonic relationship [33], which becomes the main reason for us to choose it for presenting the correlation between properties of interest and the influencing factors.

### 2.3. Dataset size test for machine learning

A dataset of sufficient size is needed to acquire stable results of a machine learning (ML) model. To establish this dataset a convergence analysis is needed. As an instance, in Supplementary Fig. 8 we presents an infrastructure of the convergence analysis on the size of a dataset, focusing on the coercivity  $H_c$ . We firstly gridded multiple dataset size  $N_1 \sim N_n$ . For each dataset size  $N_i$ , multiple cycles sampling trials are performed, forming  $N_i$  sets of nanostructural ( $L, d, w_S, w_Z$ ) as well as micromagnetic parameters ( $\alpha, M_s, l_{dw}, \sigma_{dw}$ ), and the corresponding simulated  $H_c$ . Then, the characteristic values of the dataset (DCV)  $C_{H_c}^{N_i}$  are calculated for each sampling trial. Here the arithmetic mean of simulated  $H_c$  is taken as the DCV of the dataset. Finally, using the mean of the DCV  $\langle C_{H_c}^{N_i} \rangle$  and mean absolute percentage error (MAPE)  $M_{H_c}^{N_i}$  are evaluated for the sampling dataset size  $N_i$ . The total cycles of sampling trials are labelled as  $m$ . The MAPE of all sampling trials with certain sample size  $N_i$  is defined as

$$M_{H_c}^{N_i} = \frac{|\langle C_{H_c}^{N_i} \rangle - C_{H_c}^\infty|}{C_{H_c}^\infty} \times 100\%, \quad (10)$$

where  $C_{H_c}^\infty$  represents the DCV of a sampling trial with the dataset size approaching to infinity ( $N \rightarrow \infty$ ). According to the law of large number (LLN), all  $\langle C_{H_c}^{N_i} \rangle$  of any sampling trials with  $N \rightarrow \infty$  should converge to a unified  $C_{H_c}^\infty$ . Here, we adopt the weak form of LLN and take  $M_{H_c}^{N_i} \leq 1\%$  as the convergence criterion, and the dataset size  $N_i$  at that moment as the threshold dataset size for conducting data-driven and machine-learning approaches.

Dataset Size	Sampling Trial 1		Sampling Trial 2		Sampling Trial $m$		Mean DCV of Trials	MAPE	
	dataset	DCV							
$N_1$	$H_c^{(1)}, H_c^{(2)}, \dots, H_c^{(N_1)}$	$C_{H_c}^{N_1}$	$H_c^{(1)}, H_c^{(2)}, \dots, H_c^{(N_1)}$	$C_{H_c}^{N_1}$	...	$H_c^{(1)}, H_c^{(2)}, \dots, H_c^{(N_1)}$	$C_{H_c}^{N_1}$	$\langle C_{H_c}^{N_1} \rangle$	$M_{H_c}^{N_1}$
$N_2$	$H_c^{(1)}, H_c^{(2)}, \dots, H_c^{(N_2)}$	$C_{H_c}^{N_2}$	$H_c^{(1)}, H_c^{(2)}, \dots, H_c^{(N_2)}$	$C_{H_c}^{N_2}$	...	$H_c^{(1)}, H_c^{(2)}, \dots, H_c^{(N_2)}$	$C_{H_c}^{N_2}$	$\langle C_{H_c}^{N_2} \rangle$	$M_{H_c}^{N_2}$
$N_3$	$H_c^{(1)}, H_c^{(2)}, \dots, H_c^{(N_3)}$	$C_{H_c}^{N_3}$	$H_c^{(1)}, H_c^{(2)}, \dots, H_c^{(N_3)}$	$C_{H_c}^{N_3}$	...	$H_c^{(1)}, H_c^{(2)}, \dots, H_c^{(N_3)}$	$C_{H_c}^{N_3}$	$\langle C_{H_c}^{N_3} \rangle$	$M_{H_c}^{N_3}$
...	...		...		...	...		...	...
$N_n$	$H_c^{(1)}, H_c^{(2)}, \dots, H_c^{(N_n)}$	$C_{H_c}^{N_n}$	$H_c^{(1)}, H_c^{(2)}, \dots, H_c^{(N_n)}$	$C_{H_c}^{N_n}$	...	$H_c^{(1)}, H_c^{(2)}, \dots, H_c^{(N_n)}$	$C_{H_c}^{N_n}$	$\langle C_{H_c}^{N_n} \rangle$	$M_{H_c}^{N_n}$
$\infty$							$C_{H_c}^\infty$	0	

**Supplementary Fig. 8.** Schematic of convergence analysis on the sample size of dataset. Multiple sampling trials on the simulation parameters and corresponding results were performed for every sample size  $N_i$ . Taking simulated coercive fields ( $\{H_c^{(1)}, H_c^{(2)}, \dots, H_c^{(N_i)}\}$ ) as an instance, the characteristic value of this dataset (DCV)  $C_{H_c}^{N_i}$  was calculated on each trial. This leads to the evaluation of mean DCV  $\langle C_{H_c}^{N_i} \rangle$  and the mean absolute percentage error (MAPE)  $M_{H_c}^{N_i}$  of all sampling trials for every  $N_i$ . According to the law of large number (LLN), this mean DCV supposes to converge to the true DCV (equivalently, the MAPE supposes to converge to zero) when the sample size trends to infinity.

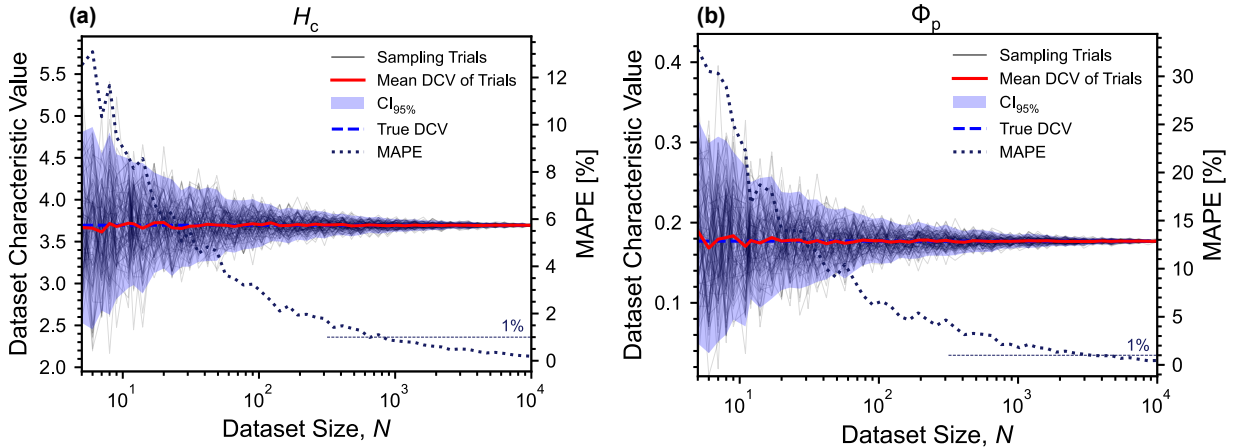
Supplementary Figure 10 shows the convergence analyses of the DCV with varying dataset sizes. It can be seen, that with an increase in the dataset size the mean DCV converges and the MAPE continuously decreases for both  $H_c$  and  $\Phi_p$ . Specifically, DCV of  $H_c$  reaches convergence after dataset size larger than 800, and DCV of  $\Phi_p$  reaches convergence after dataset size larger than 3,500. In this regard, we could conclude that the dataset size after filtering in this work (16,805) is statistically appropriate for conducting sequential data-driven and machine-learning approaches, and the representativeness of data is not affected by the sampling.

We also examined the performance of trained ML-based forward prediction models versus varying dataset size  $N$ , as Supplementary Fig. 10 presented using NN forward prediction ( $f$ -NN) model. The coefficient of determina-

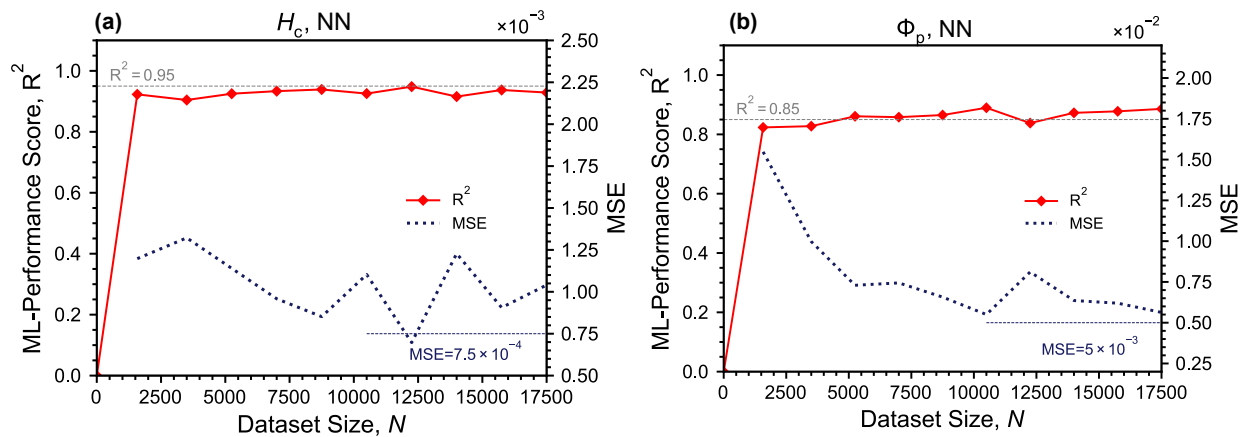
tion  $R^2$  and mean squared error (MSE). They are correspondingly defined as

$$R^2 = \frac{\sum_i^N (\hat{Y}_i - \bar{Y})^2}{\sum_i^N (Y_i - \bar{Y})^2}, \quad \text{MSE} = \frac{1}{N} \sum_i^N (Y_i - \hat{Y}_i)^2, \quad (11)$$

where  $\hat{Y}_i$  is the predicted value by the forward prediction model,  $Y_i$  is the test value from micromagnetic simulations, and  $\bar{Y}$  is the mean of the test dataset with a size  $N$ . As can be seen in Supplementary Fig. 10, for both  $H_c$  and  $\Phi_p$ ,  $R^2$  converges around 95% and 85%, respectively, after dataset size larger than 9,000. And MSEs are around  $1 \times 10^{-4}$  for  $H_c$  and  $6 \times 10^{-3}$  for  $\Phi_p$ . Further increasing the dataset size has no evident improvement in both  $R^2$  and MSE. As a conservative choice, we took the dataset size of 14,000 (around 80% of the complete dataset) for training the ML-based forward prediction models.  $R^2$  obtained of around 90% are then considered satisfactory in the training of the ML-base forward prediction model.



**Supplementary Fig. 9.** Convergence analysis on the dataset characteristic values (DCVs) versus varying dataset size  $N$ . Here the arithmetic mean of the simulated magnetic responses is selected as the dataset characteristic values, i.e., (a)  $C_{H_c}^N = \frac{1}{N} \sum_{(i)}^N H_c^{(i)}$  for the coercive field and (b)  $C_{\Phi_p}^N = \frac{1}{N} \sum_{(i)}^N \Phi_p^{(i)}$  for the pinning contribution.  $H_c^{(i)}$  and  $\Phi_p^{(i)}$  are correspondingly the coercivity and pinning contribution in the dataset. For each  $N$ , 100 sampling trials were performed with their mean and 95% confident interval ( $CI_{95\%}$ ) illustrated. The mean absolute percentage error (MAPE) of the datasets with varying  $N$  was also evaluated, where the true dataset characteristic value is estimated by LLN.



**Supplementary Fig. 10.** Convergence analysis on machine learning (ML) score versus varying dataset size  $N$ .

## References

- [1] Wang, Y. *et al.* Microstructure modification induced giant coercivity enhancement in sm(co,fe,cu,zr) permanent magnets. *Scripta Materialia* **146**, 231–235 (2018).
- [2] Maury, C., Rabenberg, L. & Allibert, C. H. Genesis of the cell microstructure in the sm(co,fe,cu,zr) permanent magnets with 2:17 type. *physica status solidi (a)* **140** (1993).
- [3] Pierobon, L. *et al.* Unconventional magnetization textures and domain-wall pinning in smco magnets. *Scientific Reports* **10** (2020).
- [4] Yan, G. *et al.* Effect of grain boundary on magnetization behaviors in 2:17 type smco magnet. *Journal of Magnetism and Magnetic Materials* **489**, 165459 (2019).
- [5] Duerrschabel, M. *et al.* Atomic structure and domain wall pinning in samarium-cobalt-based permanent magnets. *Nature Communications* **8**, 7 Seiten (2022).
- [6] Kronmüller, H. & Goll, D. Micromagnetic analysis of pinning-hardened nanostructured, nanocrystalline sm2co17 based alloys. *Scripta Materialia* **47**, 545–550 (2002).
- [7] Gutfleisch, O. *et al.* Evolution of magnetic domain structures and coercivity in high-performance smco 2:17-type permanent magnets. *Acta Materialia* **54**, 997–1008 (2006).
- [8] Liu, J., Zhang, Y., Dimitrov, D. V. & Hadjipanayis, G. Microstructure and high temperature magnetic properties of sm(co,fe,cu,zr)z (z=6.7–9.1) permanent magnets. *Journal of Applied Physics* **85**, 2800–2804 (1999).
- [9] Zhang, Y. *et al.* Evolution of microstructure, microchemistry and coercivity in 2.17 type smco magnets with heat treatment. *IEEE Transactions on Magnetics* **37**, 2525–2527 (2001).
- [10] Zhang, C. *et al.* The evolution of phase constitution and microstructure in iron-rich 2:17-type sm-co magnets with high magnetic performance. *Scientific Reports* **8** (2018).
- [11] Matthias, T. *et al.* Tem-analysis of sm(co,fe,cu,zr)z magnets for high-temperature applications. *Journal of Magnetism and Magnetic Materials* **242–245**, 1353–1355 (2002). Proceedings of the Joint European Magnetic Symposia (JEMS'01).
- [12] Yan, A., Bollero, A., Gutfleisch, O., Müller, K.-H. & Schultz, L. Melt-spun precipitation hardened sm(co, fe, cu, zr)z magnets. *Materials Science and Engineering: A* **375–377**, 1169–1172 (2004).
- [13] Song, X. *et al.* Atomic scale understanding of the defects process in concurrent recrystallization and precipitation of sm-co-fe-cu-zr alloys. *Acta Materialia* **202**, 290–301 (2021).
- [14] Song, X. *et al.* Role of nanoscale interfacial defects on magnetic properties of the 2:17-type sm-co permanent magnets. *Journal of Alloys and Compounds* **816**, 152620 (2020).
- [15] Tang, W., Zhang, Y. & Hadjipanayis, G. C. Effect of zr on the microstructure and magnetic properties of sm(cobalfe0.1cu0.088zrx)8.5 magnets. *Journal of Applied Physics* **87**, 399–403 (2000).
- [16] Jia, W. *et al.* Defects-aggregated cell boundaries induced domain wall curvature change in fe-rich sm(co,fe,cu,zr) permanent magnets. *Journal of Materials Science* **55**, 13258–13269 (2020).
- [17] Okabe, F. *et al.* Microstructures and magnetic domain structures of sintered sm(co 0.720fe0.200cu0.055zr0.025) 7.5 permanent magnet studied by transmission electron microscopy. *Materials Transactions* **47**, 218–223 (2006).
- [18] Wang, G. *et al.* Cellular structure regulation and coercivity enhancement induced by la2o3 doping in 2:17 type smco magnet. *Journal of Alloys and Compounds* **849**, 156589 (2020).
- [19] Zhou, X. *et al.* Revisiting the pinning sites in 2:17-type sm-co-fe-cu-zr permanent magnets. *Journal of Rare Earths* **39**, 1560–1566 (2021). Special Issue of Multiscale Rare Earth Crystal Materials.
- [20] Horiuchi, Y., Hagiwara, M., Endo, M., Sanada, N. & Sakurada, S. Influence of intermediate-heat treatment on the structure and magnetic properties of iron-rich sm(co,fe,cu,zr)z sintered magnets. *Journal of Applied Physics* **117**, 17C704 (2015).
- [21] Exl, L. *et al.* Labonté's method revisited: An effective steepest descent method for micromagnetic energy minimization. *J. Appl. Phys.* **115**, 17D118 (2014).
- [22] Schabes, M. E. & Bertram, H. N. Magnetization processes in ferromagnetic cubes. *Journal of Applied Physics* **64**, 1347–1357 (1988).
- [23] Furuya, A. *et al.* Semi-implicit steepest descent method for energy minimization and its application to micromagnetic simulation of permanent magnets. *IEEE Transactions on Magnetics* **51**, 1–4 (2015).
- [24] Katter, M., Weber, J., Assmus, W., Schrey, P. & Rodewald, W. A new model for the coercivity mechanism of sm/sub 2/(co, fe, cu, zr)/sub 17/magnets. *IEEE Transactions on Magnetics* **32**, 4815–4817 (1996).
- [25] Fangohr, H. *et al.* A new approach to (quasi) periodic boundary conditions in micromagnetics: The macrogeometry. *Journal of Applied Physics* **105**, 07D529 (2009).
- [26] Vansteenkiste, A. *et al.* The design and verification of mumax3. *AIP Adv.* **4**, 107133 (2014).
- [27] Leliaert, J. *et al.* Current-driven domain wall mobility in polycrystalline permalloy nanowires: A numerical study. *Journal of Applied Physics* **115** (2014).
- [28] Hernando, A., Navarro, I. & González, J. On the role of intergranular exchange coupling in the magnetization process of permanent-magnet materials. *Europhysics Letters* **20**, 175 (1992).
- [29] Lin, B., Bai, Y. & Xu, B.-X. Data-driven microstructure sensitivity study of fibrous paper materials. *Mater. Des.* **197**, 109193 (2021).
- [30] Fathidoost, M., Yang, Y., Oechsner, M. & Xu, B.-X. Data-driven thermal and percolation analyses of 3d composite structures with interface resistance. *Materials & Design* **227**, 111746 (2023).
- [31] Schneeweiss, S. Sensitivity analysis and external adjustment for unmeasured confounders in epidemiologic database studies of therapeutics. *Pharmacoepidemiol. drug saf.* **15**, 291–303 (2006).
- [32] Liu, B., Vu-Bac, N., Zhuang, X. & Rabczuk, T. Stochastic multiscale modeling of heat conductivity of polymeric clay nanocomposites. *Mech. Mater.* **142**, 103280 (2020).
- [33] Rebekić, A., Lončarić, Z., Petrović, S. & Marić, S. Pearson's or spearman's correlation coefficient-which one to use? *Poljoprivreda* **21**, 47–54 (2015).